J. Fluid Mech. (1994), vol. 270, pp. 133–174
Copyright © 1994 Cambridge University Press

Flow due to an oscillating sphere and an expression for unsteady drag on the sphere at finite Reynolds number

By RENWEI MEI

Department of Aerospace Engineering, Mechanics and Engineering Science, University of Florida, Gainesville, FL 32611, USA

(Received 1 November 1991 and in revised form 6 January 1994)

Unsteady flow due to an oscillating sphere with a velocity $U_0 \cos \omega t'$, in which U_0 and ω are the amplitude and frequency of the oscillation and t' is time, is investigated at finite Reynolds number. The methods used are: (i) Fourier mode expansion in the frequency domain; (ii) a time-dependent finite difference technique in the time domain; and (iii) a matched asymptotic expansion for high-frequency oscillation. The flow fields of the steady streaming component, the second and third harmonic components are obtained with the fundamental component. The dependence of the unsteady drag on ω is examined at small and finite Reynolds numbers. For large Stokes number, $\epsilon = (\omega a^2/2\nu)^{\frac{1}{2}} \gg 1$, in which a is the radius of the sphere and ν is the kinematic viscosity, the numerical result for the unsteady drag agrees well with the high-frequency asymptotic solution; and the Stokes (1851) solution is valid for finite Re at $\epsilon \gg 1$. For small Strouhal number, $St = \omega a/U_0 \ll 1$, the imaginary component of the unsteady drag (Scaled by $6\pi U_0 \rho_f \nu a$, in which ρ_f is the fluid density) behaves as $D_{mI} \sim (h_0 St \log St - h_1 St), m = 1, 3, 5, \ldots$. This is in direct contrast to an earlier result obtained for an unsteady flow over a stationary sphere with a small-amplitude oscillation in the free-stream velocity (hereinafter referred to as the SA case) in which $D_{1I} \sim -h_1 St$ (Mei, Lawrence & Adrian 1991). Computations for flow over a sphere with a free-stream velocity $U_0(1-\alpha_1+\alpha_1 \cos \omega t')$ at $Re = U_0 2a/\nu = 0.2$ and $St \ll 1$ show that h_0 for the first mode varies from 0 (at $\alpha_1 = 0$) to around 0.5 (at $\alpha_1 = 1$) and that the SA case is a degenerated case in which the logarithmic dependence of the drag in St is suppressed by the strong mean uniform flow.

The numerical results for the unsteady drag are used to examine an approximate particle dynamic equation proposed for spherical particles with finite Reynolds number. The equation includes a quasi-steady drag, an added-mass force, and a modified history force. The approximate expression for the history force in the time domain compares very well with the numerical results of the SA case for all frequencies; it compares favourably for the PO case for moderate and high frequencies; it underestimates slightly the history force for the PO case at low frequency. For a solid sphere settling in a stagnant liquid with zero initial velocity, the velocity history is computed using the proposed particle dynamic equation. The results compare very well with experimental data of Moorman (1955) over a large range of Reynolds numbers. The present particle dynamic equation at finite Re performs consistently better than that proposed by Odar & Hamilton (1964) both qualitatively and quantitatively for three different types of spatially uniform unsteady flows.

1. Introduction

Particle-laden flows are widely encountered in industrial and technological applications, such as pneumatic conveying systems, spray injection of liquid fuel in combustors and cyclone separators, among others. In order to predict the particulate motion, an accurate particle dynamic equation is required. At small particle Reynolds number, based on the relative velocity between the fluid and the particle, Maxey & Riley's (1983) particle dynamic equation may be adequate,

$$\tfrac{4}{3}\pi a^3\rho_p\frac{\mathrm{d}\boldsymbol{v}'}{\mathrm{d}t'} = \tfrac{4}{3}\pi a^3(\rho_p-\rho_f)\boldsymbol{g}+6\pi\rho_f\nu a(\boldsymbol{u}'-\boldsymbol{v}')+6\pi\rho_f\nu a^2\int_{-\infty}^{t'}\frac{\mathrm{d}(\boldsymbol{u}'-\boldsymbol{v}')}{\mathrm{d}\tau}\frac{\mathrm{d}\tau'}{(\pi\nu(t'-\tau'))^{\frac{1}{2}}}$$

$$+\tfrac{2}{3}\pi a^3\rho_f\frac{\mathrm{d}(\boldsymbol{u}'-\boldsymbol{v}')}{\mathrm{d}t'}+\tfrac{4}{3}\pi a^3\rho_f\frac{\mathrm{D}\boldsymbol{u}'}{\mathrm{D}t'}$$

$$= F'_{G-B}+F'_{QS}(t')+F'_H(t')+F'_{AM}(t')+F'_{FS}(t'), \tag{1}$$

where ρ_p, ρ_f, $\boldsymbol{v}'$ and $\boldsymbol{u}'$ are the densities and velocities of the particle and the fluid, a is the particle radius, ν is the kinematic viscosity of the fluid, $\boldsymbol{g}$ is the gravitational acceleration, and t' is the dimensional time. The various terms on the right-hand side of (1) are as follows: F'_{G-B} is the body force (gravity minus buoyancy); $F'_{QS}(t')$ is the Stokes drag in quasi-steady form; $F'_H(t')$ is the Basset history force (Basset 1888) in the time domain, representing the memory effect on the particle motion; $F'_{AM}(t')$ is the force due to the added mass; and the last term, $F'_{FS}(t')$, results from the acceleration of the local fluid element or the stress on the sphere owing to the undisturbed fluid flow. If the sphere moves while the free stream is steady and uniform, $F'_{FS}(t')$ is zero. Here, $\mathrm{d}/\mathrm{d}t'$ refers to the time derivative on the particle trajectory and $\mathrm{D}/\mathrm{D}t' = \partial/\partial t'+\boldsymbol{u}\cdot\boldsymbol{\nabla}'$ refers to the acceleration evaluated on the fluid trajectory. The prime in this paper denotes the dimensional quantities unless otherwise stated.

Equation (1) is valid only for a very small particle Reynolds number based on the relative velocity. For inviscid non-uniform flow over a sphere, Auton, Hunt & Prud'homme (1988) have shown that added-mass force should be expressed as $\frac{2}{3}\pi a^3\rho_f((\mathrm{D}\boldsymbol{u}'/\mathrm{D}t)-(\mathrm{d}\boldsymbol{v}'/\mathrm{d}t'))$. This correction for the added-mass force is adopted hereinafter although only spatially uniform flow will be considered in specific examples.

In many practical situations, a particle Reynolds number of order unity or larger is often encountered and equation (1) is no longer adequate. One common approach is to consider the quasi-steady force and simply neglect the history force and the added-mass force. The quasi-steady force is usually represented by using the steady state drag coefficient with instantaneous velocities (thus instantaneous particle Reynolds number),

$$F'_{QS} = \tfrac{1}{2}\rho_f\pi a^2 C_D(t')|u'(t')-v'(t)|(u'(t')-v'(t)). \tag{2a}$$

A commonly used expression for the drag coefficient is

$$C_D = \frac{24}{Re}\phi, \quad \phi = (1+0.15\,Re^{0.687}), \quad Re = |u'-v'|2a/\nu, \tag{2b–d}$$

given in Clift, Grace & Weber (1978). More accurate forms were also compiled by Clift *et al.* (1978) and they are

$$\phi = 1+\tfrac{3}{16}Re, \qquad Re \leqslant 0.01, \tag{2e}$$

$$= 1+0.1315\,Re^{0.82-0.05w}, \qquad 0.01 < Re \leqslant 20, \tag{2f}$$

$$= 1+0.1935\,Re^{0.6305}, \qquad 20 < Re \leqslant 260, \tag{2g}$$

$$= \frac{Re}{24}\times 44.005\times 10^{-1.1242w+0.1558w^2}, \qquad 260 < Re \leqslant 1500, \tag{2h}$$

where
$$w = \log_{10}\mathrm{Re}. \tag{2i}$$

Another approach has been to use the modifying coefficients C_H and C_A for the history force and the added-mass force proposed by Odar & Hamilton (1964, hereinafter referred to as OH) based on the experimentally measured unsteady drag on an oscillating sphere in a stagnant viscous liquid. The history force and added-mass force are

$$F'_H(t') = C_H\rho_f a^2(\pi\nu)^{\frac{1}{2}}\int_{-\infty}^{t'}\frac{\mathrm{d}(u'-v')}{\mathrm{d}\tau'}\frac{\mathrm{d}\tau'}{(t'-\tau')^{\frac{1}{2}}}, \tag{3a}$$

$$F'_{AM}(t') = C_A\tfrac{4}{3}\rho_f\pi a^3\frac{\mathrm{d}(u'-v')}{\mathrm{d}t'}, \tag{3b}$$

where
$$C_H = 2.88+3.12/(A_c+1)^3, \tag{4a}$$

$$C_A = 1.05-0.066/(A_c^2+0.12), \tag{4b}$$

are given by Odar (1966) and

$$A_c = (u'-v')^2\Big/\left[2a\left|\frac{\mathrm{d}(u'-v')}{\mathrm{d}t'}\right|\right] \tag{5}$$

is the acceleration parameter. This approach of representing the unsteady force has been used, for example, by Schöneborn (1975), Clift *et al.* (1978, p. 296), Tsuji, Kato & Tanaka (1991), Linteris, Libby & Williams (1991), among many others. Karanfilian & Kotas (1978) did similar experiments for $10^2 < Re < 10^4$ and $0 < A_c^{-1} < 10.5$. They found that C_H and C_A are close to the respective limiting values of 6 and 0.5, derived by Basset (1888) for creeping flows, for their experimental conditions. However the total unsteady drag does not correlate well with Re and A_c.

It was pointed out by Mei (1990) and Mei & Adrian (1992) that the modifying coefficients given by OH for the history force and the added-mass force may not be physically correct because: (i) their expression for the history force has the same integration kernel that is based on the creeping flow approximation and is not uniformly valid at non-zero Re; and (ii) their experiments were conducted only for several discrete frequencies, which are relatively high and do not cover the entire frequency domain, and the dependence of the unsteady drag on frequency was not investigated.

In the numerical study of the SA case (Mei *et al.* 1991, hereinafter referred to as MLA), dependence of the unsteady drag $\tilde{F}'_H(\omega)$ and $\tilde{F}'_{AM}(\omega)$, which are the Fourier coefficients of $F'_H(t')$ and $F'_{AM}(t')$, on ω and Re was investigated over a large range of ω. It was found that at low frequency $\tilde{F}'_H(\omega)\propto\omega$, while at high frequency $\tilde{F}'_H(\omega)\propto\omega^{\frac{1}{2}}$ as predicted by Stokes (1851) for unsteady creeping flow over a sphere. The added-mass force in the high-frequency limit was found to be the same as in the cases of potential flow and creeping flow; no modification is needed for $F'_{AM}(t')$ at low and moderate Re. For a sphere moving with velocity v' and experiencing a large mean free-

stream velocity $U'(\gg v')$ with a small unsteady fluctuations $u_1'(t') \ll U'$, Mei & Adrian (1992) obtained the following approximation for the history force in the time domain,

$$F_H'(t') = 6\pi\rho_f \nu a \int_{-\infty}^{t'} K(t'-\tau')\frac{\mathrm{d}(u_1'-v')}{\mathrm{d}\tau'}\mathrm{d}\tau' \tag{6}$$

where

$$K(t'-\tau') \approx \left\{\left[\frac{\pi(t'-\tau')\nu}{a^2}\right]^{\frac{1}{4}} + \left[\tfrac{1}{2}\pi\frac{(U'+u_1'-v')^3}{a\nu f_H^3(Re)}(t'-\tau')^2\right]^{\frac{1}{2}}\right\}^{-2}, \tag{7}$$

$$f_H(Re) = 0.75 + 0.105\,Re; \quad Re = U'2a/\nu. \tag{8}$$

This approximation was based on: (i) the numerical results of the SA case at finite Re over a wide range of frequencies; (ii) the asymptotic results at small Re and low frequency for the SA case that gives the long-time behaviour of the kernel $K(t'-\tau')$; (iii) Stokes solution for high-frequency oscillating flow over a sphere; (iv) the principle of causality (i.e. the motion of the particle can be influenced only by its previous history, not by its future behaviour); and (v) an interpolation for the imaginary component of the history force in the frequency domain. An important feature of this modified history force is that the integration kernel, $K(t'-\tau')$, decays as $(t'-\tau')^{-2}$ at large time as opposed to $(t'-\tau')^{-\frac{1}{2}}$ derived by Basset (1888). This implies that the initial condition or disturbance decays much faster at large time. The total unsteady drag on a sphere with a unidirectional relative motion, based on the results of the SA case, is therefore

$$F'(t') = \tfrac{4}{3}\pi a^3(\rho_p-\rho_f)g + 6\pi\rho_f\nu a(u'-v')\phi(t') + 6\pi\rho_f\nu a\int_{-\infty}^{t'} K(t'-\tau')\frac{\mathrm{d}(u'-v')}{\mathrm{d}\tau'}\mathrm{d}\tau'$$
$$-\tfrac{2}{3}\rho_f\pi a^3\frac{\mathrm{d}v'}{\mathrm{d}t'} + 2\rho_f\pi a^3\frac{\mathrm{D}u'}{\mathrm{D}t'}, \tag{9}$$

where $u'(t')$ is the instantaneous fluid velocity that consists of a large mean and a small fluctuation, $v'(t')$ is the velocity of the sphere with $|v'| \ll |u'|$, and $K(t'-\tau')$ is given by (6)–(8).

Strictly speaking, the kernel given by (7)–(8) is valid only for the SA case in a spatially uniform flow with a nearly constant Re. In recent parallel studies by Mei (1993) and Lawrence & Mei (1993, hereinafter referred to as LM), an unsteady flow over a stationary sphere owing to a step change in the free-stream velocity from U_1 to U_2 $(0 \leqslant U_1 \leqslant U_2)$ was investigated using a time-dependent finite-difference method for finite $Re = U_2 2a/\nu$ over a large range of time. The history force on the sphere was obtained by subtracting the steady drag from the computed total drag because $F_{AM}'(t') = 0$ for $t' > 0$. For such a singular acceleration, the numerical results indicate that the approximate expressions (6)–(8) give the correct short-time behaviour for the history force and captures qualitatively its long-time behaviour, while OH's expression (3*a*) misrepresents the history force for all time. It is also worth noting that the asymptotic and numerical results of LM showed that the history force decays as t'^{-2} at large time which supports qualitatively the long-time behaviour of $F_H'(t')$ given by (6)–(8). However, the SA case and the case involving a step change in the free-stream velocity are only two special cases of unsteady flows. They are quite different from the PO case investigated experimentally by OH. The applicability of (7)–(8) to other types of unsteady flows is not clear yet.

Lovalenti & Brady (1993*a*, hereinafter referred to as LB) obtained an expression for the hydrodynamic force on a rigid spherical particle translating with an arbitrary

velocity at low Re using a reciprocal theorem. They predicted a t'^{-2} decay for the history force at large time when a sphere suddenly accelerates from U_1 to U_2 if $U_1 = 0$. An exponential decay was found, however, for the history force for the case with $U_2 > U_1 > 0$. The general result was applied to the SA case (Lovalenti & Brady 1993*b*); the prediction for the history force agreed very well with the numerical results of MLA at small Re in the frequency domain. In the time domain, they showed that the integration kernel decays exponentially, not algebraically, for large time. However, the exponential decay of the history force over a sphere with a step change in its velocity from a non-zero initial value, $U_1 > 0$, has been shown in LM to result from the linearization of the Navier–Stokes equation in the Oseen region in LB's analysis at low Re. If the complete nonlinear effect is taken into account, a t'^{-2} decay is obtained whether or not U_1 is zero. For a sphere which impulsively reverses its direction of motion or suddenly stops its motion, both LB and LM predicted a t'^{-1} decay (with the same coefficient) for the history force. To recapitulate, the general expression for the unsteady force given by LB is very illuminating and useful in many cases; nevertheless, it is not uniformly valid for all cases even at low Re. Since we are interested in Reynolds numbers ranging from less than one to several hundred, further studies are warranted.

The main purpose of this paper is to investigate the applicability of the dynamic equation (9), as well as the history force approximations (6)–(8), to other rectilinear motions with a motivation that it may be applied to more complex unsteady multiphase flow systems with finite particle Reynolds numbers. To this end, the unsteady flow due to a sphere executing a simple harmonic oscillation at finite Re is investigated and the unsteady drag is evaluated numerically. It may appear at first that the SA case and the PO case are just subsets of a more general unidirectional unsteady flow over a sphere. However, these two cases are different in several ways which warrants the present study. First, for the SA case (MLA 1991), the history force at low frequency is strongly affected by Re which suggests that the nonlinear convection plays an important role at low frequency; it is the nonlinear convection that is responsible for $\tilde{F}'_H(\omega) \propto \omega$, instead of $\tilde{F}'_H(\omega) \propto \omega^{\frac{1}{2}}$, at small ω. However, the nonlinear convection in the SA case is dictated by the strong steady uniform flow, while that in the PO case involves the nonlinear interaction among different Fourier modes (see, for example, equation (21)). The mean flow in the PO case is induced by nonlinear streaming that is quite weak at both low and high frequencies. Thus, the history forces in two cases are expected to be different at low frequency. It turns out that the imaginary part of the unsteady drag, D_I, that is related to the history force, in the PO case has a logarithmic dependence on ω at small St and the SA case is only a degenerated case. Secondly, the flow patterns of the PO case at higher Re do not resemble that of the SA case in general. The flow reverses periodically and the sphere is under the influence of a constantly changing wake. In the experimental investigations of Temkin & Kim (1980) and Temkin & Mehta (1982), it was argued, based on a series of carefully obtained photographic measurements, that changes in the unsteady wake could affect the unsteady drag significantly. Thus the PO case also offers a unique opportunity to examine the influence of the periodically changing wake on the unsteady drag. Lastly, in terms of the solution procedures, a regular perturbation can be applied to the Navier–Stokes equation for the SA case before employing the finite-difference method. The resulting equation was linear which made the interpretation of the unsteady drag rather simple. The relevant lengthscales associated with the unsteadiness were ϵ^{-1} and Re^{-1} at high and low frequencies, respectively, in the SA case (MLA 1991; Mei & Adrian 1992). The importance of the transverse lengthscale ϵ^{-1} and the streamwise lengthscale St^{-1} as $St \to 0$ (see equation (39)) was suppressed by the strong convection

of the mean flow in the SA case; and a relatively small computational domain, $r'/a \leqslant 150$, was adequate to capture the correct low-frequency behaviour of the drag for $Re \geqslant 0.1$. For the PO case, no linearization is possible and the effect of nonlinear convection must be completely accounted for. In contrast to the SA case, ϵ^{-1} and St^{-1} are dynamically important lengthscales in the transverse and streamwise directions for the vorticity transport when $St \ll Re \ll 1$. Thus, a much larger domain, $r'/a \sim O(St^{-1})$, is needed for the PO case in order to evaluate the low-frequency force reliably.

The rest of this paper is organized as follows. In §2, the problem of the unsteady flow due to an oscillating sphere at finite Re is formulated using: (i) a 4-mode expansion in the frequency domain; and (ii) a time-dependent finite-difference method in the time domain. An asymptotic result for the unsteady drag in the high-frequency limit at finite Re is presented in §3 (solution details are given in the Appendix). In §4, results are presented and discussed. The unsteady flow fields associated with various Fourier modes are analysed in low- and high-frequency limits in §4.1. The accuracy of the numerical solutions for the unsteady drag is addressed in §4.2 by comparing with the experimental results of OH. In §4.3, the dependence of various unsteady drag components on frequency is examined; pertinent comparisons are made with the SA case. Some qualitative features of the oscillating flow at low and high frequencies are discussed. §4.4 presents detailed assessment of the proposed history force, given by expressions (6)–(8), for the PO and SA cases by comparing the analytical prediction with the numerical solution. The dynamic equation (9) is finally used to predict the velocity history of a settling sphere in a stagnant viscous liquid; the results are reported in §4.4. Excellent agreement between the prediction and the measurement of Moorman (1955) is obtained for a wide range of Reynolds number based on the terminal velocity of the sphere. To summarize, equations (6)–(8) or (55)–(56) are recommended for approximating the history force on a spherical particle. Equation (54) is recommended for computing the total unsteady drag on a sphere moving in a fluid flow for low and moderate values of Re.

2. Formulation for numerical solutions

2.1. *Governing equations*

For a sphere oscillating in a stationary fluid, the problem is equivalent to a purely oscillating flow $u'(t') = U_0 \cos \omega t'$ over a stationary sphere, provided that a force $-\frac{4}{3}\rho_f \pi a^3 (\mathrm{d}u'/\mathrm{d}t')$ is added to account for the acceleration of the fluid flow. For such an oscillating flow over the stationary sphere, the dimensionless unsteady Navier–Stokes equation in the stream function–vorticity formulation for axisymmetric flow in spherical coordinates (r, θ) is

$$St \frac{\partial g}{\partial t} + \sin\theta \left[\frac{\partial \psi}{\partial r} \frac{\partial}{\partial \theta}\left(\frac{g}{r^2}\right) - \frac{\partial \psi}{\partial \theta} \frac{\partial}{\partial r}\left(\frac{g}{r^2}\right) \right] = \frac{2}{Re} \mathscr{D}^2 g, \tag{10}$$

$$\mathscr{D}^2 \psi \equiv \left(\frac{\sin\theta}{r^2} \frac{\partial}{\partial \theta}\left(\frac{1}{\sin\theta} \frac{\partial}{\partial \theta}\right) + \frac{\partial}{\partial r}\left(\frac{\partial}{\partial r}\right) \right) \psi = g, \tag{11}$$

and the boundary conditions are

$$\psi = \frac{\partial \psi}{\partial r} = 0 \qquad \text{on } r = 1, \tag{12a}$$

$$\psi = g = 0 \qquad \text{on } \theta = 0, \pi, \tag{12b}$$

$$\psi \to \tfrac{1}{4}(\mathrm{e}^{-\mathrm{i}t} + \mathrm{e}^{\mathrm{i}t}) r^2 \sin^2\theta \quad \text{as } r \to \infty. \tag{12c}$$

It is noted that the angle θ is measured from the front stagnation point ($x = -1$) if the free stream is from left to right. Thus $(1/r\sin\theta)(\partial\psi/\partial r)$ is the tangential velocity in the clockwise direction. If θ is measured from the rear stagnation point ($x = 1$), the sign on the convection terms would be changed. Here,

$$r = r'/a, \quad t = t'\omega, \quad u = u'/U_0, \quad \psi = \psi'/(U_0 a^2), \quad \zeta = \zeta' a/U_0, \quad \mathscr{D}^2 = a^2\mathscr{D}'^2 \tag{13}$$

are the dimensionless variables and operator; ψ and ζ are the stream function and the vorticity; and

$$y = r\sin\theta, \quad g = \zeta y. \tag{14a, b}$$

The dimensionless parameters in (10),

$$Re = U_0 2a/\nu, \quad St = \omega a/U_0, \tag{15a, b}$$

are the Reynolds number and the Strouhal number. The Stokes number

$$\epsilon = (\omega a^2/2\nu)^{\frac{1}{2}} = (\tfrac{1}{4}St\,Re)^{\frac{1}{2}} \tag{15c}$$

will also be used later in analysing and presenting the unsteady flow fields and drag.

2.1.1. *Fourier mode expansion of the solution*

The main objective of solving equations (10)–(11) is to get a better understanding of the dependence of various unsteady drag components on *Re* and *St*. Thus, the method of Fourier mode expansion is first applied. The solution for $\psi(t, r, \theta)$ is first expressed in terms of the Fourier coefficients in the frequency domain as

$$\psi(r, \theta, t) = \frac{1}{2}\sum_{n=0}^{\infty}[\psi_n(r, \theta)\,e^{-int} + \psi_n^*(r, \theta)\,e^{+int}], \tag{16a}$$

where the superscript * denotes the complex conjugate. The series is then truncated at $n = 3$. Correspondingly, the function g is approximated as

$$g(r, \theta, t) \sim \frac{1}{2}\sum_{n=0}^{3}[g_n(r, \theta)\,e^{-int} + g_n^*(r, \theta)\,e^{+int}]. \tag{16b}$$

The unsteady drag is consequently

$$F(t) \sim \frac{1}{2}\sum_{n=0}^{3}[F_n\,e^{-int} + F_n^*\,e^{+int}]. \tag{17a}$$

In the present case $F_0 = F_2 = 0$, owing to the symmetry of the flow. Hence,

$$\begin{aligned} F(t) &\sim \tfrac{1}{2}[(F_{1R} + iF_{1I})\,e^{-it} + (F_{1R} - iF_{1I})\,e^{it}] \\ &\quad + \tfrac{1}{2}[(F_{3R} + iF_{3I})\,e^{-i3t} + (F_{3R} - iF_{3I})\,e^{i3t}] \\ &= \mathrm{Re}(F_1\,e^{-it} + F_3\,e^{-i3t}). \end{aligned} \tag{17b}$$

Using the Fourier mode expansion, the flow fields associated with various high-order harmonics can be obtained and investigated easily. The apparent physical interpretation of the flow field and the unsteady drag in the frequency domain is an advantage of the Fourier mode expansion. This is, however, achieved at the expense of accuracy because it seems that the convergence of (16) and (17) are not guaranteed. There are no apparent small parameters in the expansion. Physically, the above expansion should converge for small and moderate values of *Re* because the high-order harmonics are generated by the nonlinearity of the system. The energy associated with higher modes should decrease as the order of the mode increases while the first

harmonic, $[\psi_1 e^{-it} + \psi_1^* e^{it}]$, in (16) remains dominant because it is driven at infinity through the boundary condition. This method is especially useful for $\epsilon \sim O(1)$ or larger.

It should be mentioned here that this approach cannot be used for high-Reynolds-number flows, even if many terms are kept in the expansion (16), because a high-Reynolds-number flow usually has its own natural frequency, which is different from the fundamental frequency of the free-stream oscillation and the higher harmonics. The results obtained using the 4-mode expansion are thus limited to the case of low and moderately high Reynolds numbers, say $Re < 170$, so that non-harmonic terms are not present (see Kim & Pearlstein 1990).

2.1.2. *Time-dependent solution*

The second technique employed is to solve (10)–(11) in the time domain directly using a finite-difference method in both time and space. Because of the periodic flow reversal, a second-order upwind scheme (Mei & Plotkin 1986*b*) in both spatial directions (r, θ) is implemented. The time derivative is discretized using a backward Euler scheme. The wall vorticity is evaluated using Briley's (1971) formulation. The solutions are obtained iteratively owing to the nonlinearity and the coupling of the system. The flow variables at a new timestep, say $(n+1)$, are estimated first by linearly extrapolating those at $(n-1)$ and n, and are updated subsequently in each iteration within one timestep. The unsteady drag at every timestep is evaluated and stored. Fourier transformation of the unsteady drag results in various components in the frequency domain. The time-dependent approach is used here to: (i) provide an independent check on the accuracy of the Fourier mode expansion; (ii) obtain more accurate unsteady drag at very low frequency because it is found that the low-frequency drag using the Fourier mode expansion is more sensitive to the size of the computational domain than using the time-dependent approach, possibly owing to the neglect of the higher modes. More consistent results for the low-frequency drag are obtained using the time-dependent approach. The two approaches give nearly the same results for $\epsilon \sim O(1)$ or larger. The time-dependent technique is more expensive than the 4-mode expansion when the flow fields for a series of ϵ are to be obtained.

2.2. *Coordinate stretching and the transformed governing equations*

The numerical solution based on the Fourier mode expansion is performed in a domain of $1 \leqslant r \leqslant r_E$ and $0 \leqslant \theta \leqslant \frac{1}{2}\pi$ using 33 grid points in the θ-direction and 65 or 129 grid points in the r-direction. To obtain the time-dependent solution, 65 or 129 grid points are used in $0 \leqslant \theta \leqslant \pi$. The following transformation is used to cluster grid points near the surface in both approaches,

$$r = 1 + (r_E - 1)\{1 - c \tan^{-1}[(1 - x_2)\tan(1/c)]\}. \tag{18}$$

Here, x_2 is the normal coordinate in the computational domain with $0 \leqslant x_2 \leqslant 1$. In this study, either $c = 0.642$ or $c = 0.645$ is used. It was found that the imaginary component of the unsteady drag is sensitive to r_E at very small St in both 4-mode expansion and time-dependent approaches. To obtain consistent results for very small St, the flow fields for a given (Re, St) are obtained for various values of r_E and the imaginary component of the unsteady drag is obtained by extrapolating the results to $r_E \to \infty$. For $\epsilon \sim O(1)$ or larger, $r_E = 150$ for $0.2 \leqslant Re \leqslant 10$ and $r_E = 90$ for $20 \leqslant Re \leqslant 100$ are found satisfactory. See §4.3.2 for additional details.

2.2.1. *Transformed equations using Fourier mode expansion*

For the Fourier mode expansion method, computations are carried out in computational coordinates (x_1, x_2) where x_2 is as defined above and $x_1 = \theta$. Equations (16) and (17) for g_n and ψ_n in (x_1, x_2) coordinates become

$$-\mathrm{i}nSt\, g_n + h_2 \sin x_1 \left[\frac{\partial}{\partial x_1}(UG_n/y^2) + \frac{\partial}{\partial x_2}(VG_n/y^2)\right] = \frac{2}{Re}\mathscr{L}^2(g_n), \tag{19}$$

$$\mathscr{L}^2(\psi_n) = g_n, \tag{20}$$

where

$$UG_0 = u_0 g_0 + \tfrac{1}{4}(u_1 g_1^* + u_1^* g_1 + u_2 g_2^* + u_2^* g_2 + u_3 g_3^* + u_3^* g_3), \tag{21a}$$

$$UG_1 = u_0 g_1 + u_1 g_0 + \tfrac{1}{2}(u_1^* g_2 + u_2 g_1^* + u_2^* g_3 + u_3 g_2^*), \tag{21b}$$

$$UG_2 = u_0 g_2 + u_2 g_0 + \tfrac{1}{2}(u_1 g_1 + u_1^* g_3 + u_3 g_1^*), \tag{21c}$$

$$UG_3 = u_0 g_3 + u_3 g_0 + \tfrac{1}{2}(u_1 g_2 + u_2 g_1), \tag{21d}$$

(VG_n is similarly defined) and

$$\mathscr{L}^2(f) \equiv \left[\frac{\sin x_1}{r^2}\frac{\partial}{\partial x_1}\left(\frac{1}{\sin x_1}\frac{\partial f}{\partial x_1}\right) + h_2 \frac{\partial}{\partial x_2}\left(h_2 \frac{\partial f}{\partial x_2}\right)\right], \tag{22}$$

$$u_n = \frac{\partial \psi_n}{\partial x_2}, \quad v_n = -\frac{\partial \psi_n}{\partial x_1}, \tag{23}$$

$$h_2 = \frac{\partial x_2}{\partial r}. \tag{24}$$

The conditions (12*a*) are similarly expressed in the (x_1, x_2) coordinates. The conditions at infinity are

$$\psi_0 \to 0, \quad \psi_2 \to 0, \quad \psi_3 \to 0, \quad \text{and} \quad \psi_1 \to \tfrac{1}{2} r^2 \sin^2 x_2, \tag{25a}$$

$$g_n = 0, \ (n = 0, 1, 2 \text{ and } 3) \quad \text{as } r \to \infty. \tag{25b}$$

The numerical implementation for ψ_n ($n = 0$, 1, 2 and 3) at infinity exactly follows (25*a*). The conditions at $\theta = \pi$ are replaced by the following at $\theta = \frac{1}{2}\pi$ where the symmetrical and anti-symmetrical conditions for the odd and even modes are enforced,

$$\frac{\partial \psi_{2m+1}}{\partial \theta} = \frac{\partial g_{2m+1}}{\partial \theta} = 0, \quad g_{2m} = \psi_{2m} = 0, \quad (m = 0, 1) \quad \text{at } \theta = \tfrac{1}{2}\pi. \tag{26}$$

The above results from: (i) the relations between (ψ, g) and the velocity components u_θ and u_r; (ii) the fact that $u_\theta(r, \frac{1}{2}\pi - \theta, t) = -u_\theta(r, \frac{1}{2}\pi + \theta, t + \frac{1}{2}T)$ and

$$u_r(r, \tfrac{1}{2}\pi - \theta, t) = u_r(r, \tfrac{1}{2}\pi + \theta, t + \tfrac{1}{2}T)$$

for a periodically varying flow field which has also been observed in the time-dependent solution; and (iii) equations (16*a*, *b*) for the decompositions of ψ and g into various Fourier components. Here, $T = 2\pi$ is the period of the oscillation. When non-harmonic components are generated at higher *Re*, the Fourier mode expansion fails in the entire flow field and (26) is invalid consequently. An immediate consequence of (26) is that force components associated with ψ_0 and ψ_2, i.e. F_0 and F_2, are zero because the contributions to the drag from $0 \leqslant \theta \leqslant \frac{1}{2}\pi$ cancels that from $\frac{1}{2}\pi \leqslant \theta \leqslant \pi$.

It can be seen from (21) that the truncation error in (19) is due to the neglect of nonlinear interactions involving higher harmonics. This truncation error is small for flows with small *Re* or large ϵ. The results from the time-dependent solution indicate

that the dominant effect of the nonlinear interaction among different modes on the first harmonic g_1 has been captured by the terms appearing in (21) and terms such as $u_2^* g_3$, $u_3 g_2^*$, $u_3^* g_4$ and $u_4 g_3^* \ldots$ play a less important role.

In the above, g_n and ψ_n ($n = 1$, 2 and 3) are complex functions. They are expressed in terms of real and imaginary parts,

$$\psi_n = \psi_{nR} + \mathrm{i}\psi_{nI}, \tag{27a}$$

$$g_n = g_{nR} + \mathrm{i} g_{nI}. \tag{27b}$$

This results in a set of fourteen steady, strongly coupled, linear and nonlinear equations. They are solved using the approach developed by Mei & Plotkin (1986*a*) for steady problems with a relaxation factor that depends on Re.

The dimensional drag on the sphere consists of the frictional drag due to shear stress F_f' and the pressure drag F_p' due to normal stress

$$F' = F_p' + F_f'. \tag{28}$$

The relations between the dimensionless frictional drag $F_f = F_p'/\rho_f \nu U_0 a$ and the dimensionless wall vorticity $\zeta = g/y$ are

$$F_f = 2\pi \int_0^\pi \zeta|_{r=1} \sin^2\theta \, \mathrm{d}\theta, \tag{29a}$$

$$F_p = -\pi \int_0^\pi \sin 2\theta \left[\int_0^\theta \left(\frac{\partial \zeta}{\partial r} + \frac{\zeta}{r} \right)_{r=1} \mathrm{d}x_1 \right] \mathrm{d}\theta, \tag{29b}$$

where $\partial\zeta/\partial r$ for various components is computed using the values at four grid points along the radial direction with a formal third-order accuracy and the integrations are evaluated numerically using the trapezoidal rule. The unsteady drag given by (17*b*) and evaluated from the above is then scaled by $6\pi\rho_f \nu U_0 a$ to give

$$\mathscr{F}_T(t) = F'(t)/(6\pi\rho_f \nu U_0 a) = \mathrm{Re}\,[D_1(Re, St)\,\mathrm{e}^{-\mathrm{i}t} + D_3(Re, St)\,\mathrm{e}^{-\mathrm{i}3t} + \ldots], \tag{30}$$

where D_1 and D_3 may be viewed as normalized drag coefficients.

2.2.2. *Time-dependent solution*

For the time-dependent approach, the following equations

$$St \frac{\partial g}{\partial t} + h_2 \sin x_1 \left[\frac{\partial}{\partial x_1}(ug/y^2) + \frac{\partial}{\partial x_2}(vg/y^2) \right] = \frac{2}{Re} \mathscr{L}^2(g), \tag{31}$$

$$\mathscr{L}^2(\psi) = g, \tag{32}$$

are solved at every timestep in $0 \leqslant \theta \leqslant \pi$, where u, v, and h_2 are defined by (23)–(24). The second-order upwind scheme is applied to the convection terms in both x_1- and x_2-directions; the tridiagonal solver (Anderson, Tennehill & Fletcher 1984) is used in the radial direction. The initial condition for (g, ψ) is the steady solution at the same Re. At $r = r_E$, $g = 0$ is set. Since the velocity at infinity is $\cos(t)$, ψ at $r = r_E$ is specified as $\psi(r = r_E) = \frac{1}{2}\cos(t) r_E^2 (1 - r_E^{-3}) \sin^2 x_2$. To solve for ψ efficiently, $\psi(r, \theta, t)$ is decomposed into a potential flow component ψ_p and a viscous component ψ_v as

$$\psi = \psi_p(r, \theta, t) + \psi_v(r, \theta, t), \tag{33}$$

with

$$\psi_p(r, \theta, t) = \tfrac{1}{2}\cos(t) r^2 (1 - r^{-3}) \sin^2 x_2, \tag{34}$$

and

$$\mathscr{L}^2(\psi_v(r, \theta, t)) = g, \quad \psi_v(r = 1) = 0, \quad \psi_v(r = r_E) = 0. \tag{35}$$

With this decomposition, a large change in ψ caused by the change in the free-stream velocity $\cos(t)$ and large r_E^2 results in only a small change in $\psi_v(r, \theta, t)$ from one timestep to another.

The forces F_f and F_p are evaluated using (29). Fourier transformation is applied to the time series of the unsteady drag beyond the initial transient. If the unsteady drag at $t = t_1 + 2\pi$ is the same as that at $t = t_1$ within four decimal places, the data after t_1 is considered to be uncontaminated by the initial transient. For very low frequency, this t_1 is not large (typically less than a few dozen timesteps for $\Delta t = \pi/150$) because the initial acceleration at $t = 0$ in the free stream is zero and the history effect is small. For larger values of St, it takes a few cycles to reach a steady oscillatory flow; thus the drag for high-frequency oscillation is obtained using the 4-mode expansion technique instead.

3. Asymptotic solution for the unsteady drag in an oscillating flow at finite Reynolds number and high frequency

In Mei & Adrian (1992), the Stokes solution, which is valid for $Re \ll 1$ and finite ϵ, was used to represent the high-frequency unsteady drag at finite Re. A similar approach was used by Riley (1966) in studying the second-order steady streaming induced by an oscillating flow over a stationary sphere. Landau & Lifshitz (1959) also suggested that the Stokes solution for the unsteady drag can be used for the high-frequency oscillating flow. However, no rigorous analysis has been given to justify the use of the Stokes solution for the unsteady drag at finite Re and high frequency for an oscillating flow over a sphere and the arguments usually given are *ad hoc*.

Wang (1968) investigated the high-frequency oscillatory flow over a stationary cylinder at finite Re. For $St^{-1} < Re < St$, one boundary layer with a thickness of $O((Re\,St)^{-\frac{1}{2}})$ can be identified near the surface of the cylinder. A matched asymptotic expansion was used to obtain inner and outer solutions of the oscillating and the steady components of the stream function. Following closely the procedure developed by Wang (1968) for the cylinder, the solution to the oscillating flow over a sphere can be obtained. Since the technical details are the same as that given in Wang (1968), only the final result for the unsteady drag is given here. The governing equations in terms of the stream functions, and the definitions for various terms, and the solutions to those terms are given in the Appendix.

From (A 31) in the Appendix, the unsteady drag (defined by (17*a*)) at high frequency associated with the fundamental frequency can be easily obtained to $O(1)$ by computing the pressure and frictional components given by (29),

$$F_1' e^{-it}/(6\pi\rho_f \nu U_0 a) = D_{1B} e^{-it}$$

$$= e^{-it}[-\tfrac{2}{3}i\epsilon^2 + \epsilon(1-i) + 1] \quad \text{for finite } Re \text{ and } \epsilon \gg 1, \tag{36}$$

or

$$D_{1BR} \to 1 + \epsilon, \tag{37a}$$

$$D_{1BI} \to -(\epsilon + \tfrac{2}{3}\epsilon^2) \quad \text{for finite } Re \text{ and } \epsilon \gg 1. \tag{37b}$$

The subscript B denotes that the present asymptotic solution for finite Re coincides with the corresponding Basset's (1888) solution in the time domain or the Stokes (1851) solution in the ω-domain for $Re \ll 1$. Thus the use of the Stokes unsteady drag solution for high frequency at finite Re is justified. The leading-order term of D_{1B}, $-i\frac{2}{3}\epsilon^2$, is the added-mass force, $-i\frac{2}{9}\epsilon^2$, plus that due to the free-stream acceleration, $-i\frac{4}{9}\epsilon^2$. By comparing (37) with the Stokes solution, the $O(\epsilon)$ term in D_{1B}, $(1-i)\epsilon$, can be identified

here as the history force at finite Re in the large ϵ limit. The $O(1)$ term in D_{1B} is exactly 1, that is independent of Re because the nonlinear convection only has higher-order effects at large ϵ. The implication of this $O(1)$ term will be discussed later.

4. Results and discussions

4.1. *Flow fields analysis for various modes*

In this part, we examine the flow fields in three different limits: (*a*) the quasi-steady limit $St = 0$; (*b*) the low Reynolds number, low-frequency limit with $St \ll Re < 1$; and (*c*) the high-frequency limit with $\epsilon \sim O(1)$ or larger. A better understanding on the unsteady flow field is essential to the understanding of the unsteady drag behaviour. The low-frequency flow to be presented is obtained using the time-dependent approach while the quasi-steady and high-frequency flow field is obtained using 4-mode expansion.

4.1.1. *Quasi-steady flow*

In the limit $St \to 0$, the imaginary part of $g_n(r, \theta)$ defined in (16*b*) vanishes. The function g can be expressed in terms of the real components g_{nR} as

$$g(r, \theta, t) = \sum_{n=0}^{\infty} g_{nR}(r, \theta) \cos(nt) \quad (St \to 0). \tag{38}$$

At any t, $g(r, \theta, t; Re, St = 0)$ should represent the steady result $g(r, \theta)$ at $Re(t) = Re\cos(t)$ if (38) is accurate. Figure 1 compares two types of wall vorticity at $Re(t) = 10$, 20, 40 and 100: (i) that from the steady state solution; and (ii) that given by (38) with $\cos(t) = 0.1$, 0.2, 0.4 and 1 with $g_{nR}(r, \theta)$ ($n = 0$, 1, 2 and 3) computed at $Re = 100$. The steady flow fields are computed first at $Re = 10$, 20, 40 and 100 with free-stream velocity $U_\infty = 1$ and are subsequently re-scaled by the instantaneous free-stream velocity $U_\infty = \cos(t)$. They are compared with the corresponding quasi-steady results. The 4-mode expansion is seen to give a wall vorticity that is in close agreement with the steady state results for $\cos(t) = 0.2$, 0.4 and 1. For the wall vorticity at $Re(t) = 10$ based on $Re = 100$ and $\cos(t) = 0.1$, the relative error is not small. This suggests that: (i) more terms in the expansion in (16*b*) are needed to represent accurately the wall vorticity at $Re(t) = 10$ using the results obtained for $Re = 100$; (ii) four terms are adequate for $Re(t) = 20$ and sufficient for $Re(t) \geqslant 40$ (or higher) in the Fourier mode expansion based on the results for $Re = 100$. Nevertheless, since the absolute error between the quasi-steady and steady results at $\cos(t) = 0.1$ is not large and the time span for $|\cos(t)| \leqslant 0.1$ only constitutes about 6.4% of the period, the overall error is small when the error is averaged over an entire period for $0 \leqslant Re(t) \leqslant Re = 100$. The four Fourier modes are thus adequate to describe quasi-steady flows even at $Re = 100$ in terms of the wall vorticity.

It must be mentioned also that when the streamlines were plotted, the shapes of the separation bubble were not exactly the same for $Re(t) = 40$ (based on the quasi-steady solution at $Re = 100$ and $\cos(t) = 0.4$) and $Re = 40$ of the steady solution. This is because the values of the stream function near the separation region are very small and sensitive to errors, which implies that more terms are needed in (16) to represent accurately the quasi-steady flow field at various instantaneous Reynolds numbers.

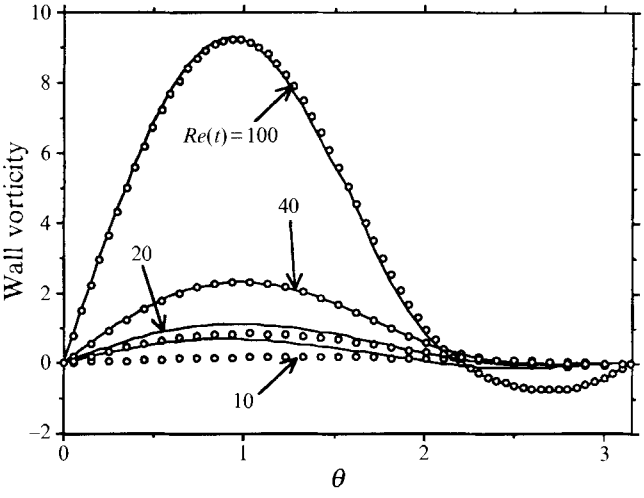

FIGURE 1. Comparison of the instantaneous wall vorticity for an oscillating flow with $Re = 100$ and $St = 0$ at $Re(t) = 10$, 20, 40 and 100 between ○, the steady solution and ——, the quasi-steady solutions obtained using 4-mode expansion.

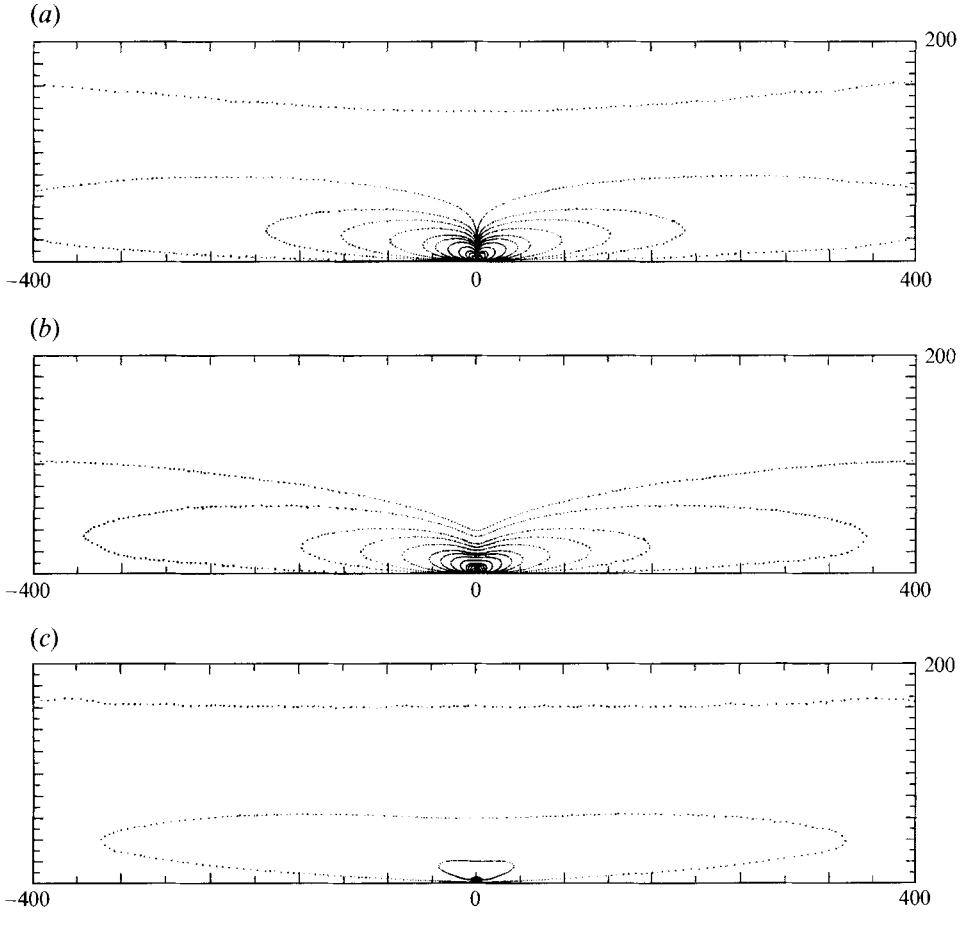

FIGURE 2. Contours of the Fourier components of the vorticity at $Re = 1$, $St = 0.002$ in a purely oscillating flow, $-400 \leqslant x \leqslant 400$, $0 \leqslant y \leqslant 200$. (*a*) ζ_0; (*b*) ζ_{1R}; and (*c*) ζ_{1I}.

4.1.2. *Low-frequency flow when $St \ll Re$: interpretation of the numerical results and a qualitative asymptotic analysis for $St \ll Re \ll 1$*

To understand the behaviour of the unsteady drag, especially the imaginary components, at low frequency when $St \ll Re$, it is instructive to examine the gross feature of the flow field associated with various Fourier modes. From the time-dependent solutions, the first two Fourier components of the stream functions, $\psi_0(r,\theta)$, $\psi_{1R}(r,\theta)+i\psi_{1I}(r,\theta)$, and the vorticity, $\zeta_0(r,\theta)$, $\zeta_{1R}(r,\theta)+i\zeta_{1I}(r,\theta)$ can be obtained by using Fourier transformation over a period of oscillation. To see the flow induced by the oscillation, the imposed flow, $\frac{1}{2}r^2\sin^2\theta$, is subtracted from the first mode which leaves $\delta\psi_{1R}(r,\theta) = \psi_{1R}(r,\theta) - \frac{1}{2}r^2\sin^2\theta$. Figure 2 shows the contours of $\zeta_0(r,\theta)$, $\zeta_{1R}(r,\theta)$ and $\zeta_{1I}(r,\theta)$ for $Re = 1$, $St = 0.002$ ($\epsilon = 0.00236$) in the region: $0 \leqslant y = r\sin\theta \leqslant 200$, $-400 \leqslant x = r\cos\theta \leqslant 400$. The results are obtained using 65×129 grids with $r_E = 1200$, $c = 0.645$, and a timestep size $\Delta t = \pi/150$. The important feature is that all three contours are very elongated far away from the sphere. This suggests that the relevant lengthscale in the streamwise (x) direction is much larger than the lengthscale in the transverse (y) direction in the far away region. For the SA case (MLA 1991), it was shown that the relevant lengthscale in the region far away from the sphere for $St \ll Re \ll 1$ is the Oseen lengthscale Re^{-1}. Apparently, this is not the case in the PO case: these three components of the vorticity extend to regions far larger than $r \sim Re^{-1}$. The large extent of the vorticity is obviously caused by the absence of a strong mean convection in the PO case.

Figure 3 shows the contours of $\psi_0(r,\theta)$, $\delta\psi_{1R}(r,\theta)$ and $\psi_{1I}(r,\theta)$ for $Re = 1$, $St = 0.002$ in the same region: $0 \leqslant y \leqslant 200$, $-400 \leqslant x \leqslant 400$. From figure 3($a$), it is seen that the steady streaming, $\psi_0(r,\theta)$, extends to a very large region, although it is quite weak at small St. In figure 3(b), the streamlines of $\delta\psi_{1R}(r,\theta)$ exhibit a significantly elongated structure produced by the oscillating sphere. The disparity in the lengthscales in the x- and y-directions is also clear; and it is consistent with the earlier observation for $\zeta_{1R}(r,\theta)$. Figure 3(c) shows the imaginary component $\psi_{1I}(r,\theta)$ that is much weaker than $\delta\psi_{1R}(r,\theta)$. Clearly, $\psi_{1I}(r,\theta)$ behaves like a uniform flow in the region $0 \leqslant y \leqslant 100$, $-400 \leqslant x \leqslant 400$. This uniform flow behaviour of $\psi_{1I}(r,\theta)$ at large distance is responsible for the imaginary component of the drag D_{1I}. It is also seen that further away the streamlines of $\psi_{1I}(r,\theta)$ appear closed and the contours are quite elongated. Figure 3(d) shows $\delta\psi_{1R}(r,\theta)$ for $Re = 0.2$, $St = 0.002$. Comparing with figure 3(b), the flow structures are seen to be similar except that the scale in the transverse direction for $Re = 1$ ($\epsilon = 0.02236$) is only a fraction of that for $Re = 0.2$ ($\epsilon = 0.01$).

To understand further the different lengthscales in the x- and y-directions, $\delta\psi_{1R}(r,\theta)$ and $\psi_{1I}(r,\theta)$ at $\theta = \pi/64$ (the first grid line away from the centreline or x-axis) and $\theta = \frac{1}{2}\pi$ (transverse direction) are compared at a given $St\,(= 0.002)$ with two different Stokes numbers: $\epsilon = 0.01$ ($Re = 0.2$) and $\epsilon = 0.02236$ ($Re = 1$). Figure 4(a) shows $\delta\psi_{1R}(r,\theta = \pi/2)$ and $\delta\psi_{1R}(r,\theta = \pi/64)$ at these two Stokes numbers. For a given St, $\delta\psi_{1R}(r,\theta = \pi/64)$ does not change with Re or ϵ and it peaks at the same location, $r \sim O(St^{-1})$. This clearly suggests that the lengthscale in the streamwise direction is $l_x = St^{-1}$. On the other hand, $\delta\psi_{1R}(r,\theta = \pi/2)$ decreases with increasing ϵ and the peak location of $\delta\psi_{1R}(r,\theta = \pi/2)$ is roughly correlated with ϵ^{-1}. This suggests that the relevant lengthscale in the y-direction is $l_y = \epsilon^{-1}$. Figure 4(b) shows the imaginary component, $\psi_{1I}(r,\theta = \pi/2)$ and $\psi_{1I}(r,\theta = \pi/64)$, at $\epsilon = 0.01$ and 0.02236. It is seen that the peak location of $\psi_{1I}(r,\theta = \pi/64)$ is at $r \sim O(St^{-1})$ and $\psi_{1I}(r,\theta = \pi/64)$ depends mainly on St. In the transverse direction, the peak of $\psi_{1I}(r,\theta = \pi/2)$ is reduced with

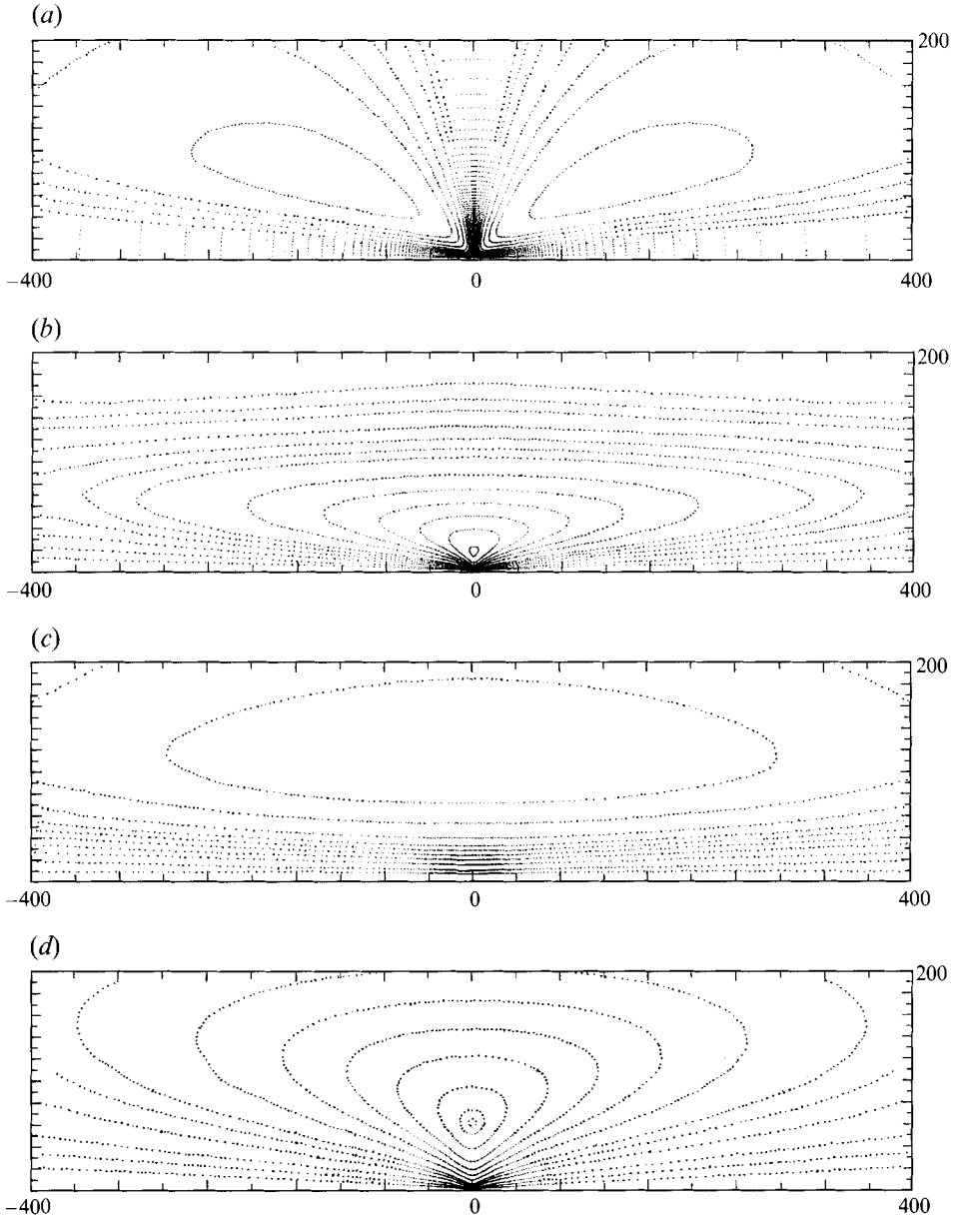

FIGURE 3. Contours of the Fourier components of the stream function at $Re = 1$, $St = 0.002$ in a purely oscillating flow, $-400 \leqslant x \leqslant 400$, $0 \leqslant y \leqslant 200$. (*a*) ψ_0; (*b*) $\delta\psi_{1R}$; (*c*) ψ_{1I}; and (*d*) $\delta\psi_{1R}$ at $Re = 0.2$, $St = 0.002$.

increasing ϵ and the peak location seems to correlate with ϵ^{-1}. It is interesting, however, that for $r < 20$ $\psi_{1I}(r, \theta = \pi/2, \epsilon = 0.01)$ and $\psi_{1I}(r, \theta = \pi/2, \epsilon = 0.02236)$ are nearly the same. All four curves in figure 4(*b*) have a slope of 2 in the log–log coordinates. Hence in the region $r \ll \epsilon^{-1}$, ψ_{1I} is again independent of ϵ and the flow field of ψ_{1I} in $r \ll O(\epsilon^{-1})$ is a uniform flow over the sphere. Although $Re = 1$ is not small, the asymptotic feature of the flow fields is quite similar to that of $Re \ll 1$. For $St \ll Re \ll 1$ ($Re \ll 1$ in the asymptotic sense), this uniform flow extends beyond the Oseen region $r \sim O(Re^{-1})$ because $\epsilon \ll Re$.

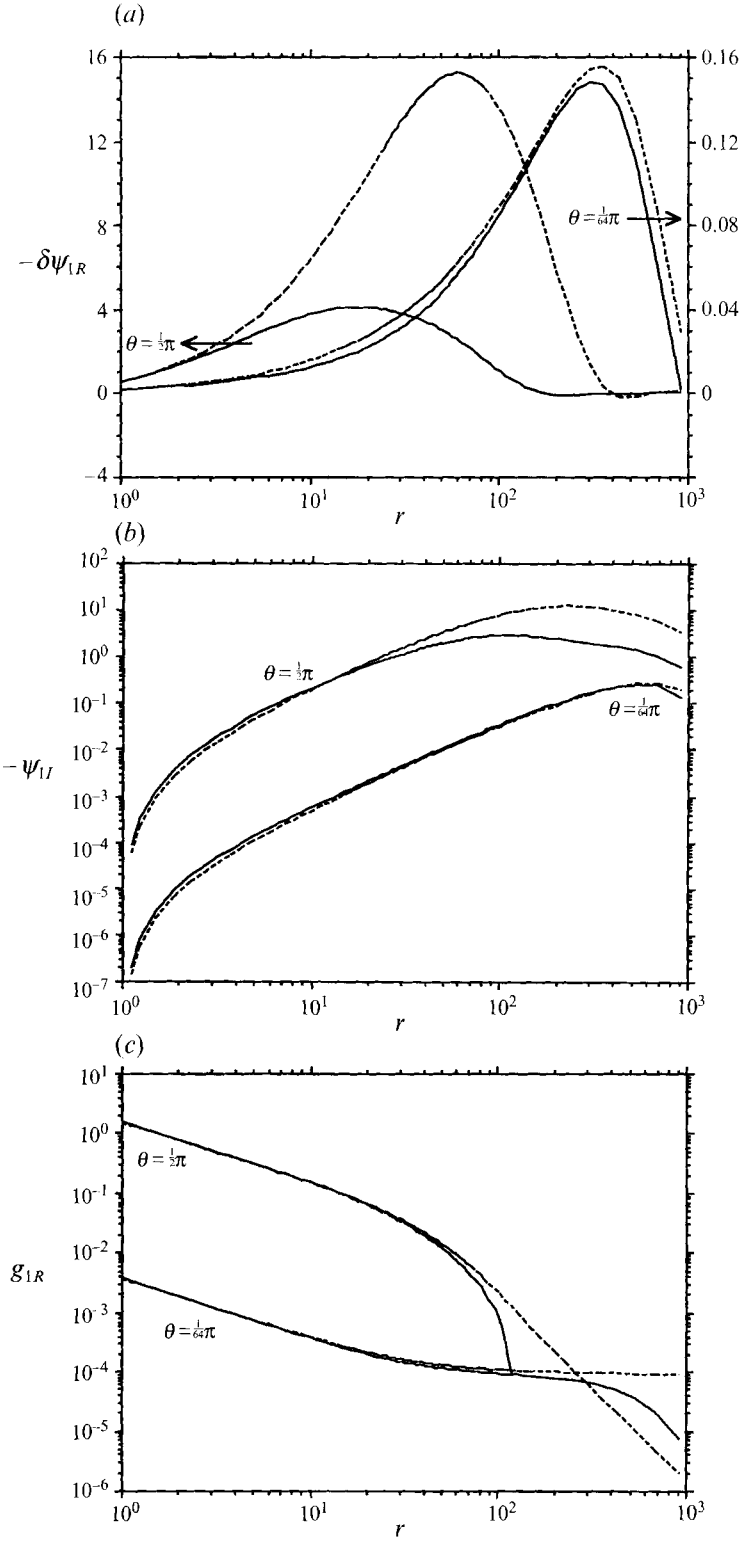

FIGURE 4. For caption see facing page.

The reason why $l_y = \epsilon^{-1}$ is easy to comprehend; it arises from balancing the unsteady term by the cross-stream diffusion term in the unsteady Navier–Stokes equation. The streamwise lengthscale, $l_x = St^{-1}$, must result from the balance between the unsteady term and the convection term in the Navier–Stokes equation in the region $r \sim O(St^{-1})$ where the viscous effect is quite small for $St \ll Re$. Using

$$X = x/l_x = xSt, \quad Y = y/l_y = y\epsilon, \tag{39}$$

to rescale equation (10), the leading-order equation for the vorticity transport in the region where $x \sim O(St^{-1})$ and $y \sim O(\epsilon^{-1})$ can be derived as

$$\frac{\partial g}{\partial t} + \cos(t)\frac{\partial g}{\partial X} = \tfrac{1}{2}Y\frac{\partial}{\partial Y}\left(\frac{1}{Y}\frac{\partial g}{\partial Y}\right). \tag{40}$$

Thus the vorticity transport far away from the sphere is governed by an unsteady convection–diffusion process that is similar to an unsteady laminar wake. The convection is in the streamwise direction with a time varying speed. The diffusion is in the transverse direction only. Owing to the retaining of the unsteady term, the vorticity and stream function decay and oscillate spatially for $X \gg 1$ and $Y \gg 1$, as shown in figure 4(*a*). These important dynamic features in the region $r \gg Re^{-1}$ are absent in the SA case (see Mei & Adrian 1992) owing to the strong mean convection that confines the vorticity to the Oseen region of size $r \sim O(Re^{-1})$.

How is the flow field in the outer region of $x \sim O(St^{-1})$ and $y \sim O(\epsilon^{-1})$ connected to the flow field closer to the particle? Now consider the Oseen region, $r \sim O(Re^{-1})$, which we may call an 'intermediate' region. Using $\rho = rRe' = \frac{1}{2}rRe$, $X' = xRe'$, we can obtain, for $St \ll Re \ll 1$,

$$\cos(t)\frac{\partial g}{\partial X'} = \mathscr{D}_\rho^2 g \tag{41}$$

to the leading order. In the above, the operator $\mathscr{D}_\rho^2$ is similar to $\mathscr{D}^2$ defined by (11) with ρ replacing r in the Oseen region. This is the quasi-steady Oseen equation for $g = \zeta r \sin\theta$; and t is only parametrically important, not dynamically. Because $Y = r\epsilon = \rho\epsilon/Re'$, the solution to (41) should not be valid for $\rho \sim Re'/\epsilon \gg 1$ when $Y \sim O(1)$. Instead, it should join the solution to (40) for large ρ but small Y. Further toward the particle, there is the well-known Stokes region, $r \sim O(1)$, or inner region. The dynamic equation for $r \sim O(1)$ is the quasi-steady Stokes equation

$$0 = \mathscr{D}^2 g. \tag{42}$$

Thus, the flow field at $St \ll Re \ll 1$ has a triple-region structure: an inner region $r \sim O(1)$, an intermediate region $r \sim O(Re'^{-1})$, and an outer region $x \sim O(St^{-1})$, $y \sim O(\epsilon^{-1})$. It is also worth commenting that for large $Re \sim 1$, the inner and intermediate regions will be altered to accommodate the Prandtl boundary layer of thickness $Re^{-\frac{1}{2}}$. However, the outer region, $x \sim O(St^{-1})$ and $y \sim O(\epsilon^{-1})$, is unaffected by a finite Re.

FIGURE 4. (*a*) Comparisons of $\delta\psi_{1R}(r, \theta = \frac{1}{2}\pi)$ and $\delta\psi_{1R}(r, \theta = \pi/64)$ at fixed St (= 0.002) between ---, $\epsilon = 0.01$ ($Re = 0.2$) and ——, $\epsilon = 0.02236$ ($Re = 1$) for the PO case. Note that the lengthscales for $\delta\psi_{1R}$ are ϵ^{-1} at $\theta = \frac{1}{2}\pi$ (transverse direction) and St^{-1} at $\theta = \pi/64$ (streamwise direction), respectively. (*b*) Comparisons of $\psi_{1I}(r, \theta = \frac{1}{2}\pi)$ and $\psi_{1I}(r, \theta = \pi/64)$ at fixed St (= 0.002) between ---, $\epsilon = 0.01$ ($Re = 0.2$) and ——, $\epsilon = 0.02236$ ($Re = 1$) for PO case. Note that, for $St \ll \epsilon \ll Re < 1$, $\psi_{1I}(r, \theta = \pi/64)$ along the streamwise direction depends on St for $r < O(St^{-1})$ while $\psi_{1I}(r, \theta = \frac{1}{2}\pi)$ along the transverse direction depends on St for $r < O(\epsilon^{-1})$. (*c*) Comparisons of $g_{1R}^{QS}(r, \theta)$ and $g_{1R}(r, \theta)$ at $\theta = \pi/64$ and $\theta = \frac{1}{2}\pi$ for $Re = 0.2$, $St = 0.002$. ---, the quasi-steady solution and ——, the numerical solution to the full Navier–Stokes equation agree in the Oseen region $r \sim O(Re^{-1})$.

To see how these three regions join, we turn to the matched asymptotic solution, which is uniformly valid in the Stokes and Oseen regions, obtained by Proudman & Pearson (1957) for steady flow. For the quasi-steady oscillating flow, the leading-order solution for the vorticity related function, g, is

$$\begin{aligned} g^{QS}(t,r,\theta) &= \mathscr{D}^2\psi^{QS}(t,r,\theta) \\ &= -\frac{3}{4}\left(Re'+\frac{2}{r}\right)\sin^2\theta\cos(t)\exp[-\tfrac{1}{2}Re'r|\cos(t)|(1-\cos\theta)]\} \quad \text{if } \cos(t)>0 \\ &= -\frac{3}{4}\left(Re'+\frac{2}{r}\right)\sin^2\theta\cos(t)\exp[-\tfrac{1}{2}Re'r|\cos(t)|(1+\cos\theta)]\} \quad \text{if } \cos(t)<0. \end{aligned} \tag{43}$$

Fourier transformation,

$$g_{1R}^{QS}(r,\theta) = \frac{1}{\pi}\int_0^{2\pi} g^{QS}(t,r,\theta)\cos t\,\mathrm{d}t,$$

yields the first Fourier component of $g_{QS}(t,r,\theta)$. It is noted that $g_{1I}^{QS}(r,\theta)=0$ because the quasi-steady flow is antisymmetrical with respect to time. Figure 4(*c*) compares $g_{1R}^{QS}(r,\theta)$ with its numerical counterpart $g_{1R}(r,\theta)$ for $\theta=\pi/64$ and $\pi/2$ for $Re=0.2$ ($Re'=0.1$) and $St=0.002$ with $\epsilon=0.01$. It is clearly seen that $g_{1R}^{QS}(r,\theta)$ agrees very well with the finite difference result, $g_{1R}(r,\theta)$, for $r<50$. In the transverse direction, $r\sim 50$ corresponds to $\rho\sim 5\gg 1$ and $Y\sim 0.5\ll 1$, respectively, in the asymptotic sense. It is thus consistent with the discussion preceding equation (42). It should be pointed out that $g_{1R}^{QS}(r,\theta=\pi/2)$ decays algebraically at $\rho\gg 1$ although $g^{QS}(t,r,\theta=\pi/2)$ decays exponentially for $|\cos(t)|>0$. This algebraic decay can be shown, using an asymptotic integration to result from the contribution near $t=\frac{1}{2}\pi$ and $t=\frac{3}{2}\pi$ when $\cos(t)=0$ in the Fourier transformation. The agreement between the quasi-steady solution and the numerical solution to the full Navier–Stokes equation in the intermediate Oseen region shows that the foregoing qualitative description for the asymptotic structure of the flow field is correct.

It must be emphasized that, for $St\ll\epsilon\ll Re\ll 1$ in the PO case, the drag D_{1I} is determined by the strength of ψ_{1I} in the region $Re^{-1}\ll r\ll\epsilon^{-1}$ in which ψ_{1I} appears as a uniform flow. For the SA case, the lengthscale $l_y=\epsilon^{-1}$ is not important for $\epsilon\ll 1$ (Mei & Adrian 1992); the unsteady term in the vorticity transport equation can be treated as a regular perturbation. The mechanism for the generation of ψ_{1I} in the region $r\gg Re^{-1}$ is thus not the same as in the PO case. It is therefore not surprising to see in §4.2 that the behaviour of D_{1I} in the two cases is not the same either.

4.1.3. *High-frequency flow*

In the foregoing discussions, the importance of the lengthscales, $l_x=St^{-1}$ and $l_y=\epsilon^{-1}$, are illustrated in the asymptotic limit $St\ll\epsilon\ll Re\ll 1$. Next, we consider flow field in the limit $St^{-\frac{1}{2}}\ll 1$ for finite Re (under restriction $St^{-1}<Re<St$) by using the asymptotic solution given in the Appendix and the 4-mode expansion. For $St^{-\frac{1}{2}}\ll 1$ with finite Re, we have $\epsilon^{-1}\ll 1$. Equation (A 14) shows that the relevant lengthscale in the Stokes layer is actually $l_r=\epsilon^{-1}$, not $St^{-\frac{1}{2}}$, although $\delta=St^{-\frac{1}{2}}$ is used as the small parameter in defining the gauge functions to facilitate the asymptotic expansion.

When the conditions $St^{-\frac{1}{2}}\ll 1$ and $Re<St$ are satisfied, g_1 given by (A 31) agrees very well with the 4-mode expansion result, as expected. In order to show further the scaling of the flow field with ϵ at high frequency, we consider the case for $\epsilon>1$, $St^{-\frac{1}{2}}<1$

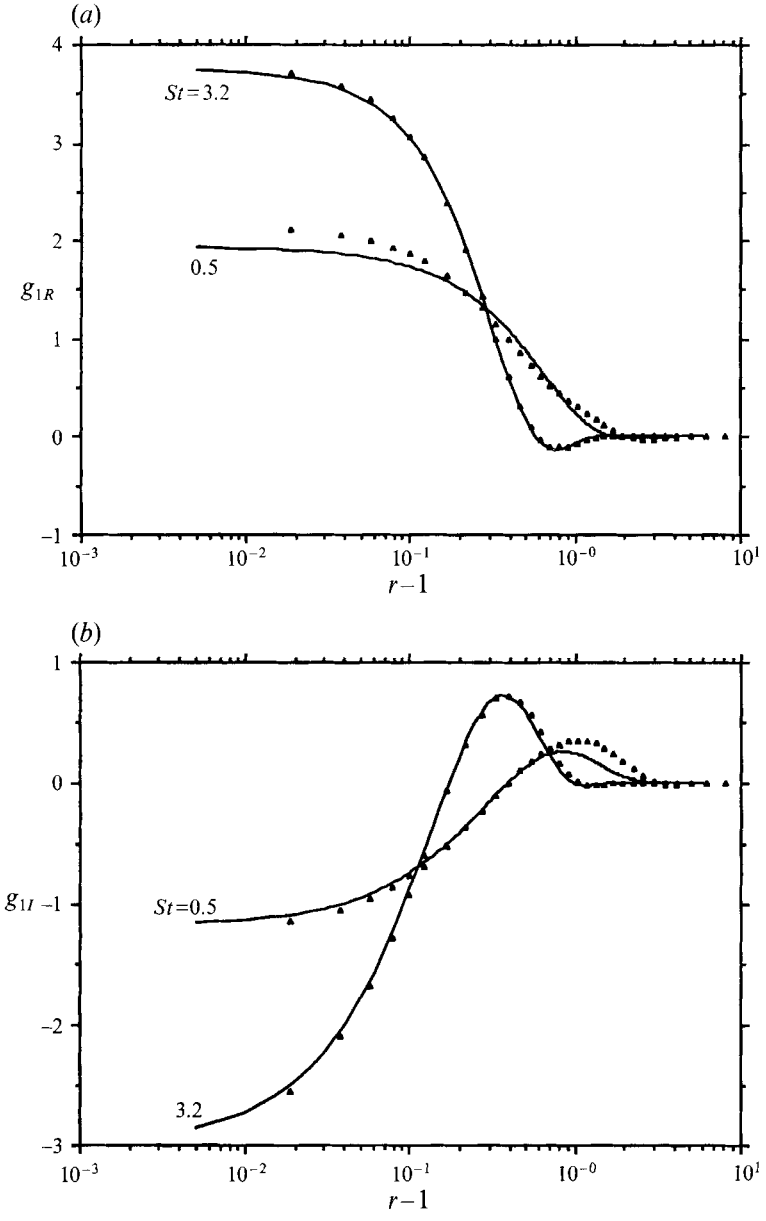

FIGURE 5. Comparisons of the real and imaginary parts of g_1 between the asymptotic solution and numerical solution using 4-mode expansion at $Re = 20$, $St = 0.5$ and $St = 3.2$. (*a*) Real component; (*b*) imaginary component. ——, Asymptotic solution; ▲, 4-mode expansion.

or ~ 1, but $Re > St$ instead of $Re > St$. Figures 5(*a*) and 5(*b*) compare the real and imaginary parts of g_1 between that given by (A 31) and that computed from the 4-mode expansion at $Re = 20$, $St = 0.5$ ($\epsilon = 1.5811$) and $St = 3.2$ ($\epsilon = 4$). Noting that $\delta = 3.2^{-\frac{1}{2}} = 0.559$ is not quite small, $Re = 20$ is not small, and furthermore the condition $Re < St$ is not satisfied, the agreement between the asymptotic (3-term) and the numerical solutions for $St = 3.2$ is remarkable. In this case, $\epsilon = 4$ so that a thin Stokes layer of size $r \sim \epsilon^{-1} = 0.25$ is clearly defined and the flow outside the Stokes layer is a potential flow. This shows that the more relevant parameter in the high-

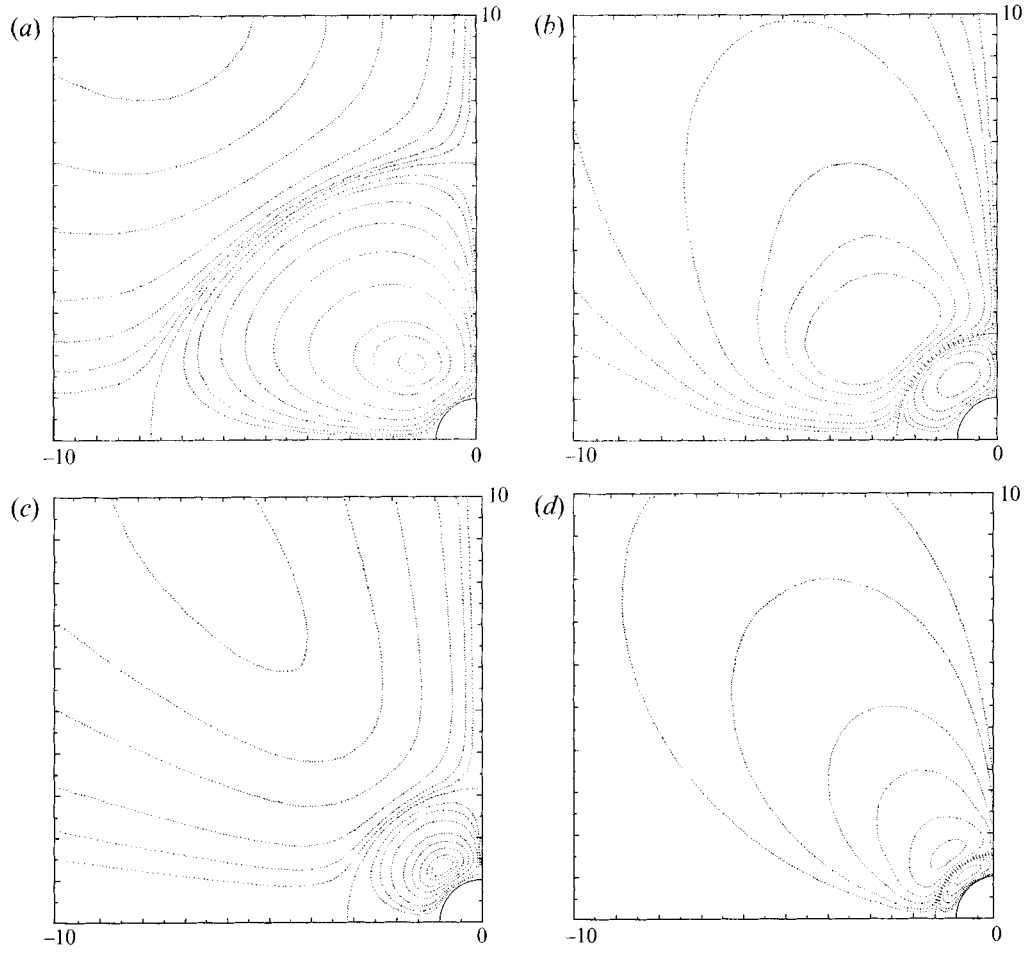

FIGURE 6. (*a*), (*b*) Streamlines of ψ_0 and ψ_{2R} at $Re = 20$, $\epsilon = 1.58$; (*c*), (*d*) streamlines of ψ_0 and ψ_{2R} at $Re = 20$, $\epsilon = 4$.

frequency flow is the Stokes number ϵ. For $St = 0.5$, $\delta = 1.414$ is not considered as small and $\epsilon = 1.5811$ is not considered as large. However, the qualitative feature of g_1 has been captured by the asymptotic solution that is supposed to be valid only for $\delta \ll 1$. The qualitative agreement can be attributed to the fact that $\epsilon > 1$ is satisfied. The discrepancy in g_{1R} lies mainly in the wall region; it arises because the asymptotic solution for g_1 neglects the nonlinear term completely while the numerical solution at $St = 0.5$ does pick up a contribution from the nonlinear convection term in the Navier–Stokes equation. The smaller the St, the larger the discrepancy. At very low frequency, the nonlinear term becomes significant and the asymptotic solution fails.

The above comparison between the 4-mode expansion result and the asymptotic result for the fundamental mode is excellent. However, it is noted that the three-term asymptotic expansion for the fundamental mode involves only the boundary-layer flow and the displacement and curvature effects. It does not involve the nonlinear contribution to g_1 from the steady streaming and the second harmonic terms.

Figure 6 shows the flow pattern of the steady component, $\psi_0(r, \theta)$, known as the steady streaming pattern and $\psi_{2R}(r, \theta)$ for $(Re, \epsilon) = (20, 1.58)$ and $(20, 4)$. The information about $\psi_{2R}(r, \theta)$ cannot be easily obtained experimentally. The steady

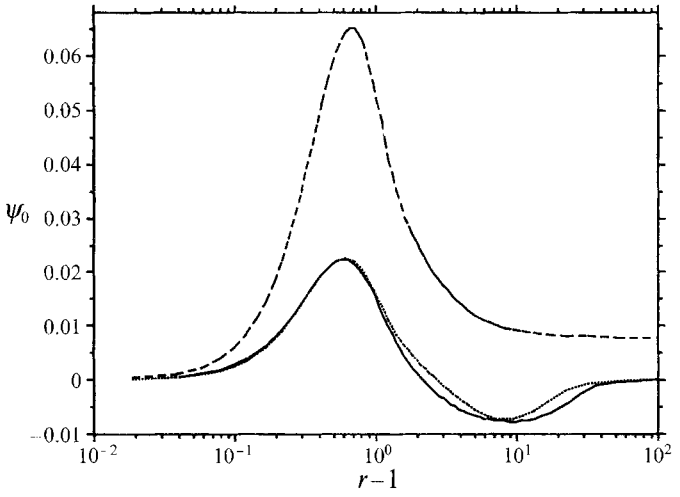

FIGURE 7. Stream function ψ_0 at $\theta = \frac{1}{4}\pi$, $Re = 20$, $\epsilon = 4$, $St = 3.2$. Solutions are obtained using ——, 4-mode expansion; ...., time-dependent solution averaged over one period; – – –, asymptotic solution for high frequency.

component, $\psi_0(r, \theta)$, for $(Re, \epsilon) = (20, 1.58)$ was also obtained by Drummond & Lyman (1990) through averaging over one period in a time-dependent computation using a coarser grid in a smaller domain. From the streamline plots of $\psi_0(r, \theta)$ and $\psi_{2R}(r, \theta)$ at $\epsilon = 4$, a Stokes layer of thickness $O(\epsilon^{-1})$ is clearly observed. The steady streaming pattern extends further away from the sphere than $\psi_{2R}(r, \theta)$ that is mainly confined in the Stokes layer. This agrees qualitatively with the asymptotic behaviour described earlier.

A closer examination of $\psi_0(r, \theta)$ at $Re = 20$ and $\epsilon = 4$ reveals that, in contrast to the fundamental mode for which the numerical and asymptotic results agree very well, the asymptotic solution over-predicts the strength of the steady streaming at $(Re, \epsilon) = (20, 4)$. This implies that the asymptotic state for high-order harmonics has not been reached. Figure 7 compares $\psi_0(r, \theta)$ at $\theta = \pi/4$ at $(Re, \epsilon) = (20, 4)$ based on: (i) a 4-mode expansion; (ii) a time-dependent solution averaged over one period; and (iii) the asymptotic solution. The two numerical solutions are close to each other while the asymptotic solution is $2 \sim 3$ times larger. This large discrepancy is caused by the neglect of the high-order terms in solving for $\bar{\psi}_0$ with a not-so-small $\delta = St^{-\frac{1}{2}} = 0.56$. The violation of the condition $Re < St$ may also contribute to the discrepancy. At high values of St, the discrepancy becomes smaller. However, accurate numerical solution for $\psi_0(r, \theta)$ is difficult to obtain owing to the thin boundary layer and a significant potential flow region for ψ_0 outside the Stokes layer, although the solution for $\psi_1(r, \theta)$ is very accurate. An important conclusion from the foregoing discussion is that, in the (Re, ϵ) parameter space, when the asymptotic solution becomes accurate for the fundamental mode, the high-order harmonics and steady streaming component may not yet be accurate. Our primary focus is on the unsteady drag that is mainly dictated by the fundamental mode. Therefore the asymptotic solution at high frequency is quite useful and the use of the Stokes solution for the unsteady drag at finite Re and large Stokes number is justified.

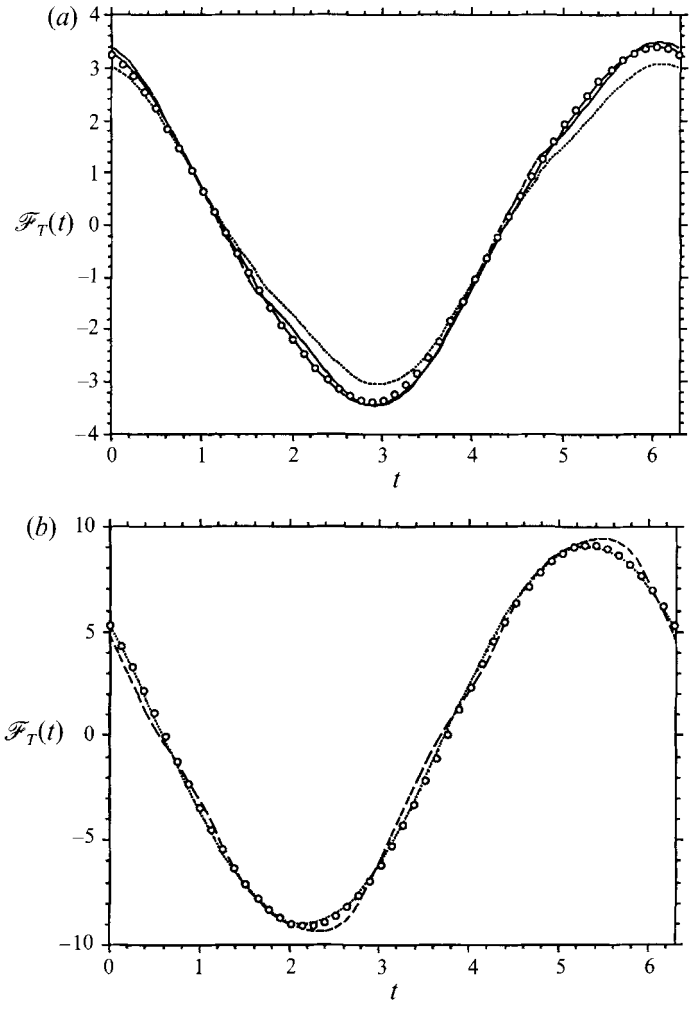

FIGURE 8. Comparison of the total unsteady drag between ---, OH's result; present numerical results: ○, 4-mode expansion; ——, time-dependent solution; and ...., prediction using the proposed form for the PO case. (*a*) $(Re, \epsilon) = (40, 1.0)$; (*b*) $(Re, \epsilon) = (40, 4.0)$.

4.2. *Comparison of the total unsteady drag and quasi-steady drag; validity of the 4-mode expansion*

To assess the accuracy of the 4-mode expansion given by (16*b*), the total unsteady drag obtained from the numerical solution given by (30) is compared with the time-dependent solution and the results of OH at $(Re, \epsilon) = (40, 1)$. The OH expression for the total unsteady drag in the PO case, equations (2*a–c*) and (3)–(5), is derived from and therefore tested against the experimentally measured values. The total unsteady drag as a function of time given by their expression at $(Re, \epsilon) = (40, 1)$ is thus reliable. For a sphere oscillating with a dimensionless velocity,

$$V = \cos(t), \tag{44}$$

in a quiescent fluid, the total dimensionless drag is

$$\mathscr{F}_T(t) \equiv F'_T(t)/(6\pi\rho\nu_f U_0 a) = \mathscr{F}_{QS} + \mathscr{F}_H + \mathscr{F}_{AM}, \tag{45}$$

where $\mathscr{F}_{QS}$, $\mathscr{F}_H$ and $\mathscr{F}_{AM}$ are the dimensionless counterparts of F'_{QS}, F'_H and F'_{AM} normalized by $6\pi\rho\nu_f U_0 a$. The OH expression (denoted by the superscript OH below) leads to the following,

$$\mathscr{F}_{QS}^{OH}(t) = \mathscr{F}_{QS}(t) = \phi(t)\cos(t), \tag{46}$$

$$\mathscr{F}_{H}^{OH}(t) = \tfrac{1}{2}C_H\epsilon[\cos(t) - \sin(t)], \tag{47}$$

$$\mathscr{F}_{AM}^{OH}(t) = -C_A\tfrac{4}{9}\epsilon^2\sin(t), \tag{48}$$

with $\phi(t)$ given by (2*e–i*). The total force based on OH's correlation is thus $\mathscr{F}_T^{OH}(t) = \mathscr{F}_{QS}^{OH}(t) + \mathscr{F}_H^{OH}(t) + \mathscr{F}_{AM}^{OH}(t)$. The numerical solution based on the 4-mode expansion (denoted by the superscript $4m$ below) gives the total force as

$$\mathscr{F}_T^{4m}(t) \sim D_{1R}\cos(t) + [D_{1I} + \mathrm{i}\tfrac{4}{9}\epsilon^2)]\sin(t) + D_{3R}\cos(3t) + D_{3I}\sin(3t). \tag{49}$$

In the above, the term $-\mathrm{i}\frac{4}{9}\epsilon^2$ is subtracted from D_{1I} because D_{1I} is the result for an oscillating flow over a stationary sphere and $-\mathrm{i}\frac{4}{9}\epsilon^2$ is the force due to the free-stream acceleration. The time-dependent solution (denoted by the superscript 'time' below), after subtracting $-\mathrm{i}\frac{4}{9}\epsilon^2\sin(t)$, gives the total force $\mathscr{F}_T^{time}(t)$ in the time domain. Figure 8(*a*) compares $\mathscr{F}_T^{OH}(t)$, $\mathscr{F}_T^{4m}(t)$, and $\mathscr{F}_T^{time}(t)$ at $(Re, \epsilon) = (40, 1)$. It can be seen that $\mathscr{F}_T^{4m}(t)$ and $\mathscr{F}_T^{time}(t)$ agree very well with each other and they both agree well with $\mathscr{F}_T^{OH}(t)$. Another test for $(Re, \epsilon) = (40, 4)$ is shown in figure 8(*b*) and good agreement is observed for higher ϵ between $\mathscr{F}_T^{OH}(t)$ and $\mathscr{F}_T^{4m}(t)$. Hence, the first four modes retained in the expansion (16*b*) give a satisfactory total drag at moderate and large values of ϵ.

As another confirmation of 4-mode expansion, the computed quasi-steady drag at $\epsilon = 0$ and finite Re is compared with that given by (2). In the limit $\epsilon \to 0$, the history force and the added-mass force approach zero. The quasi-steady drag can then be obtained from the numerical solution as

$$\begin{aligned}\mathscr{F}_{QS}^{4m}(t) &\sim D_{1R}(Re, \epsilon = 0)\cos(t) + D_{3R}(Re, \epsilon = 0)\cos(3t) + \ldots \\ &= D_{1QS}(Re)\cos(t) + D_{3QS}(Re)\cos(3t) + \ldots.\end{aligned} \tag{50}$$

The comparisons between $\mathscr{F}_{QS}^{4m}(t)$, $\mathscr{F}_{QS}^{time}(t)$, and the empirically based $\mathscr{F}_{QS}(t)$ using (2*e–i*) and (46) are shown in figure 9(*a*) for $Re = 20$, 100 and 200. Very close agreement can be observed. To measure the difference between $\mathscr{F}_{QS}^{4m}(t)$ and $\mathscr{F}_{QS}(t)$, the standard L_2-norm over one period of the oscillation is evaluated,

$$Err_2 = \|\mathscr{F}_{QS}^{4m}(t) - \mathscr{F}_{QS}(t)\|_2 / \|\mathscr{F}_{QS}^{rm}(t)\|_2. \tag{51}$$

For $Re = 20$ and 200, the relative error is 2% and 5.7%. For $Re = 0.1$, $Err_2 = 0.0035$ because the nonlinear effect is very small. For $Re = 200$, a true quasi-steady flow may not be realizable owing to the flow instability. Kim & Pearlstein (1990) found an asymmetrical instability at $Re \sim 173$ through a linear stability analysis for a steady flow past a sphere. The inclusion of $Re = 200$ in figure 9(*a*) merely shows the extent of the comparison and does not address the issue of actual flow instability.

To determine whether or not the four modes retained in the Fourier mode expansion account properly for the nonlinear interaction, the Fourier transformation (FT) of the empirically based $\mathscr{F}_{QS}(t)$ is used to assess further the accuracy of the 4-mode expansion. The FT of $\mathscr{F}_{QS}(t)$ gives a series of coefficients, a_n $(n = 0, 1, \ldots)$, that decrease with increasing n. The first two non-zero coefficients, a_1 and a_3, are approximately equal to $D_{1QS}(Re)$ and $D_{3QS}(Re)$. The third coefficient, a_5, gives an estimate for $D_{5QS}(Re)$ that has been neglected in the 4-mode expansion. Figure 9(*b*) compares the steady state drag $D_S(Re)$, numerical values of $D_{1QS}(Re)$ and $D_{3QS}(Re)$ for the PO case and the non-

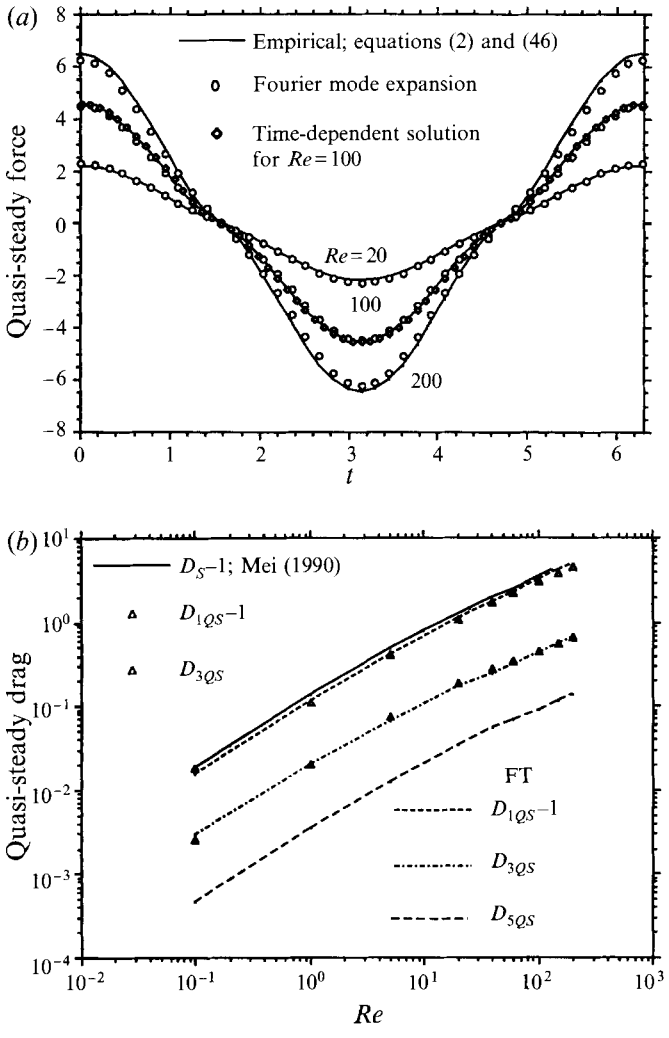

FIGURE 9. (*a*) Comparison of the quasi-steady drag $\mathscr{F}_{QS}(t)$ between the numerical results and the empirically based predictions at $Re = 20$, 100 and 200 in the PO case. (*b*) Comparison of the quasi-steady drag coefficients of various modes between the numerical results (symbols) and the results from the Fourier transformation of the empirical expression (lines).

zero coefficients of the FT, a_1, a_3, and a_5. Good agreement between $D_{1QS}(Re)$ and a_1 and between $D_{3QS}(Re)$ and a_3 can be seen for $0.1 \leqslant Re \leqslant 200$. Hence the nonlinear interactions among the first few modes can be properly represented using the 4-mode expansion.

As ω increases, D_{1R} and D_{1I} increase and approach the limits given by the high-frequency asymptotic solution. On the other hand, the numerical results show that D_{3R} decreases with increasing ω and D_{3I} increases from zero to a small value that depends on Re, and then decreases with increasing ω. In terms of its magnitude, $D_3 = (D_{3R}^2 + D_{3I}^2)^{\frac{1}{2}}$ attains a maximum at $\omega = 0$. As ω increases, the higher modes ($n \geqslant 5$) will contribute even less. Therefore, it is proper to discuss the unsteady drag by focusing on the first mode.

4.3. *Dependence of the unsteady drag on frequency in the PO case*

The total drag $\mathscr{F}_T^{OH}(t)$ was based on experimental measurements and is reliable; its decomposition into three components, $\mathscr{F}_{QS}$, $\mathscr{F}_H$ and $\mathscr{F}_{AM}$, is sound. However, their functional forms and the corrections, C_H and C_A, may not be physically sound. In deriving C_H and C_A, OH subtracted $\mathscr{F}_{QS}(t)$ from the total unsteady drag and determined C_A by the drag at $t = \frac{1}{4}\pi$ when the assumed history force $\mathscr{F}_H$ is 0. A value of $C_H = 2.88$ was then obtained at $t = \frac{1}{2}\pi$ when $\mathscr{F}_{AM} = 0$. Dependence of C_H on the acceleration parameter A_c was determined at other instants. However, the corrections do not approach to the respective limiting values of $C_H = 6$ and $C_A = 0.5$ for finite ϵ in the limit $Re \to 0$. In this limit, the Stokes solution is known to be valid for finite ϵ.

As in the SA case, the frequency-dependent part of the unsteady drag can be obtained by subtracting the quasi-steady drag $D_{1QS}(Re)$ from the total unsteady drag. Since the third harmonic drag component D_3 decreases rapidly with increasing frequency the drag associated with the first harmonic will be the main focus.

4.3.1. *Unsteady drag at intermediate and high frequencies: $\epsilon \sim O(1)$ or larger*

As shown by (36), the leading-order term of the unsteady drag at high frequency is the added-mass force, $-\mathrm{i}\frac{2}{9}\epsilon^2$, plus the force due to the free-stream acceleration, $-\mathrm{i}\frac{4}{9}\epsilon^2$. Rivero, Magnaudet & Farbe (1991) carried out an elegant numerical procedure to separate the contributions to the total unsteady force from the history force and the instantaneous added-mass force. The analysis of an oscillating flow and a uniformly accelerating flow demonstrated that the added-mass force is the same as in potential flow. Figure 10(*a*) shows the imaginary component D_{1I}, obtained from the 4-mode expansion, for 'moderate' and 'large' values of ϵ at $Re = 0.2$ and 40. The asymptotic limit $-\mathrm{i}\frac{2}{3}\epsilon^2$ can be clearly identified. This is the same as in the SA case (MLA 1991). Therefore no modification is necessary for $\mathscr{F}_{AM}(t)$ at finite Re for the oscillating flow. Subtracting $-\mathrm{i}\frac{2}{3}\epsilon^2$ from the imaginary component of the total drag, as was done in the SA case, the first imaginary component of the history force, D_{1IH}, in the entire frequency domain is obtained: $D_{1IH} = D_{1I} - (-\mathrm{i}\frac{2}{3}\epsilon^2)$. In the large ϵ limit, $D_{1IH} \sim -\mathrm{i}\epsilon$. Figure 10(*b*) compares D_{1IH} of the PO case at $Re = 0.2$ and 40 with that of the SA case. It is seen that D_{1IH}, normalized by the amplitude of the oscillation in both cases, reaches the asymptotic limit at smaller ϵ in the PO case than in the SA case; and that D_{1IH} of the PO case is larger than D_{1IH} of the SA case. The low-frequency behaviour of D_{1I} or D_{1IH} will be further discussed later.

The frequency-dependent part, or acceleration-dependent part, of the first real component drag is evaluated by subtracting the quasi-steady drag at $\epsilon = 0$ from the total drag

$$D_{1RAC}(Re, \epsilon) = D_{1R}(Re, \epsilon) - D_{1QS}. \tag{52}$$

The real component does not involve the added-mass force. Following the study for the SA case (MLA 1991), D_{1RAC} is identified here as the first real component of the history force in the frequency domain. The Stokes solution or the Basset solution for the history force gives $D_{1BRAC} = \epsilon$. Figure 10(*c*) indicates that $D_{1RAC} < D_{1BRAC} = \epsilon$ for all ϵ and $D_{1RAC} \to D_{1BRAC} = \epsilon$ for large ϵ. Thus the history force given by Basset (1888) in the time domain overestimates the actual values at large time for the PO case. The result for D_{1RAC} at very small ϵ should be interpreted with caution because of the loss of numerical accuracy in subtracting two close, approximate numbers. Although D_{1RAC} of the PO case is larger than D_{1RAC} of the SA case for all ϵ, the differences for D_{1RAC} and D_{1IH} between the SA case and the PO case are not large for moderate values

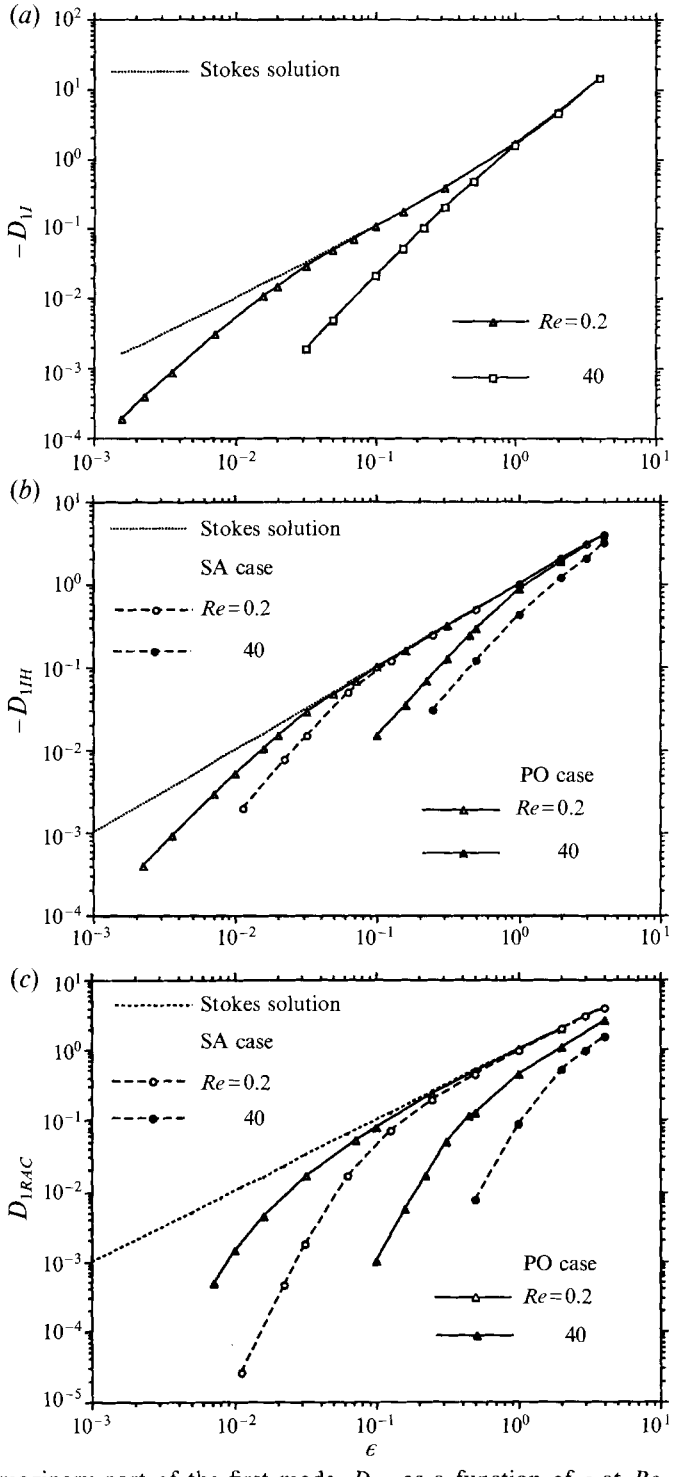

FIGURE 10. (*a*) Imaginary part of the first mode, D_{1I}, as a function of ϵ at $Re = 0.2$ and 40. (*b*) $D_{1IH} = D_{1I} - i\frac{2}{3}\epsilon^2$ as a function of ϵ at $Re = 0.2$ and 40. (*c*) $D_{1RAC} = D_{1R} - D_{1R}(\epsilon = 0)$ as a function of ϵ at $Re = 0.2$ and 40.

of ϵ and quite small for large ϵ. This suggests that when (6)–(8) are used for the PO case, the error for the history force will not be too large. This point will be discussed in §4.4.

The high-frequency asymptotic solution for the PO case shows that after the history force and the added-mass force are subtracted from D_{1B}, the $O(1)$ term left is exactly 1. The definition (52) thus leads to $D_{1BRAC} = 1 - D_{1QS}(Re) + \epsilon$. Because $D_{1QS}(Re) > 1$ for $Re > 0$, it is seen that D_{1BRAC} is less than the actual history force $D_{1RH} \sim \epsilon$ at large ϵ by an $O(1)$ quantity $D_{1QS}(Re) - 1 \sim \phi - 1$. Note that since the higher harmonics of the drag at large ϵ is quite small, it is appropriate to discuss the history force by focusing on the first mode. However, the expression for the history force given by (6)–(8) does not include this $O(1)$ difference because the expression was obtained from the imaginary component and the principle of causality. This has the following implications. If one accepts that $\mathscr{F}_{QS}(t)$ be represented by (2) and $\mathscr{F}_{AM}(t)$ be represented by the potential flow solution, then the history force must include such an $O(1)$ quantity for small time. On the other hand, if one uses the potential flow solution for $\mathscr{F}_{AM}(t)$ and Basset (1888) solution or (6)–(8) for $\mathscr{F}_H(t)$ at small time, that are asymptotically correct as shown by the analysis given in the Appendix, then this difference, $D_{1QS} - 1$, should be taken into account in the quasi-force $\mathscr{F}_{QS}(t)$. For many practical applications of interest, particle Reynolds number is not very large (say, Re below several hundred). The amount of over-prediction, $\phi - 1$, in $\mathscr{F}_{QS}(t)$ is then small in comparison with $\mathscr{F}_{AM}(t)$ and even $\mathscr{F}_H(t)$ for a highly accelerating flow; and we should not be too concerned with this error in applying equation (9).

4.3.2. *Low-frequency behaviour: $St \ll \epsilon \ll 1$*

In the SA case, D_{1I} in the low-frequency limit is proportional to St. This motivates us to examine the behaviour of $D_{mI}/St\,(m = 1, 3, \ldots)$ as functions of St at a given Re. Figure 11 shows $|D_{mI}|/St$ for $m = 1$, 3 and 5 for $Re = 0.2$ and $St \ll 1$. In direct contrast to the SA case in which $D_{1I}/St = -0.75$ (D_{1I} is already normalized by the oscillation amplitude; see Mei & Adrian 1992) as $Re \to 0$, the PO case exhibits a logarithmic dependence of $|D_{mI}|/St$ on St for all three modes. In particular,

$$D_{1I}/St \sim h_0 \log St - h_1 \quad \text{for } St \ll 1, \tag{53}$$

with $h_0 \sim 0.486$ and $h_1 \sim -0.446$ at $Re = 0.2$. It is observed that all three modes have $h_0 \sim 0.5$ within the scattering of the data. All numerical results shown in figure 11 are obtained using $r_E = 1200$, $c = 0.645$. Recall that $\psi_{1I}(r, \theta = \pi/64)$ peaks at $r \sim St^{-1}$ for $St \ll 1$ as shown in figure 4(*b*), a domain of $r_E = 2/St$ is needed (M. R. Maxey, private communication 1993) to capture accurately the spatial variation of ψ_{1I} which in turn determines D_{1I}. The results for $St > 0.001$ are obtained using a 65×129 grid and are shown in figure 11. The unsteady drag for $St \leqslant 0.001$ is first obtained from a series of computations using $r_E = 300$, 600 and 1200 on a 129×257 grid; these results at given St and Re are then extrapolated to $1/r_E \to 0$. The extrapolated values of D_{1I} as $1/r_E \to 0$ for very small St are joined with the rest of the data for larger St. Although a little scattering in the data is visible owing to numerical errors, the logarithmic dependence of D_{1I}/St on St spans over three decades. The fact that all three modes exhibit, to some extent, such behaviour reinforces the logarithmic dependence of D_{mI}/St on St to the leading order in St.

Having established, numerically, the logarithmic dependence of D_{mI} on St, it is instructive to see if the analytical expression of LB exhibits the same behaviour at low Re. The time history of the force on an oscillating sphere is thus computed using equation (6.15) of LB at $Re = 0.2$ over a range of St. The long time result is then Fourier transformed to obtain D_{mI} in the frequency domain. The first three non-zero

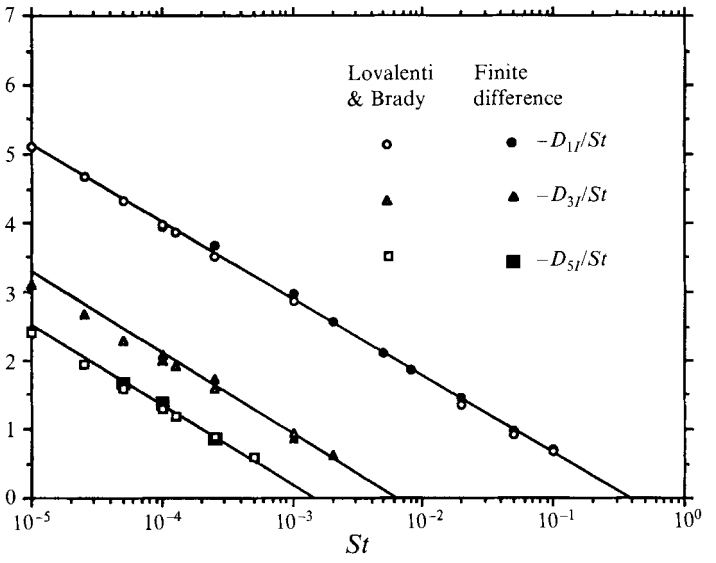

FIGURE 11. Low-frequency behaviour of D_{1I}, D_{3I} and D_{5I} at $Re = 0.2$ in the purely oscillating flow. All three components exhibit the dependence on $St \log St$ to the leading order in St as $St \to 0$. Solid symbols denote the present numerical results; open symbols denote the results obtained from Lovalenti & Brady's (1993*a*) analysis at low Re.

modes, D_{1I}/St, D_{3I}/St and D_{5I}/St, based on LB's expression are shown in figure 11 (denoted by open symbols) together with the finite-difference results. Close agreement is observed for all three modes between the analytical and numerical results. This lends further support to the logarithmic dependence of the drag on St in the PO case at low Re.

In fact, the logarithmic dependence is not just limited to small Re flows, as shown in figure 12(*a*) for D_{1I}/St as a function of St for $0.2 \leqslant Re \leqslant 40$. To examine more clearly the effect of Re on D_{1I}, the dependence of h_0 and h_1 on Re is shown in figure 12(*b*) for $0.2 \leqslant Re \leqslant 40$. It is observed that h_0 levels off at higher Re while h_1 increases almost linearly with Re for $Re \geqslant 1$. This suggests that at higher Re, the linear dependence of D_{1I} on St is overwhelming while the logarithmic dependence is relatively weaker. The data presented in figure 10(*c*) for D_{1RAC} in the small St limit indicate that $D_{1RAC} \propto St^2 \log St$ to the leading order in St for both $Re = 0.2$ and $Re = 40$. The results are not shown here because the data in figure 10(*c*) for small St are believed to contain larger errors than those in D_{1I}.

The main differences between the PO case and the SA case in the low-frequency limit are now clear. However, it is more important and revealing to see how these two different limiting cases are related and how the leading-order behaviour of D_{1I} changes from $D_{1I} \sim O(St)$ in the SA case to $D_{1I} \sim O(St \log St)$ in the PO case. To address this question, we consider an oscillating flow with a finite-amplitude fluctuation imposed on a mean stream, $U_\infty = U_0(1 - \alpha_1 + \alpha_1 \cos t)$, in which α_1 ($0 \leqslant \alpha_1 \leqslant 1$) is the amplitude parameter. Numerical results are obtained for $Re = 0.2$ over a large range of St for each α_1. Again, the logarithmic dependence, $D_{1I} \sim h_0\, St \log St - h_1\, St$, is observed in the leading order as $St \to 0$. However, h_1 can not be determined as accurately as h_0 because $O(St)$ is a high-order term in D_{1I}; hence the behaviour of h_1 should be interpreted only qualitatively. Figures 13(*a–b*) show the dependence of h_0 and h_1 on the oscillating amplitude α_1. For $\alpha_1 < 0.5$, h_0 decreases exponentially fast as $\alpha_1 \to 0$, which indicates

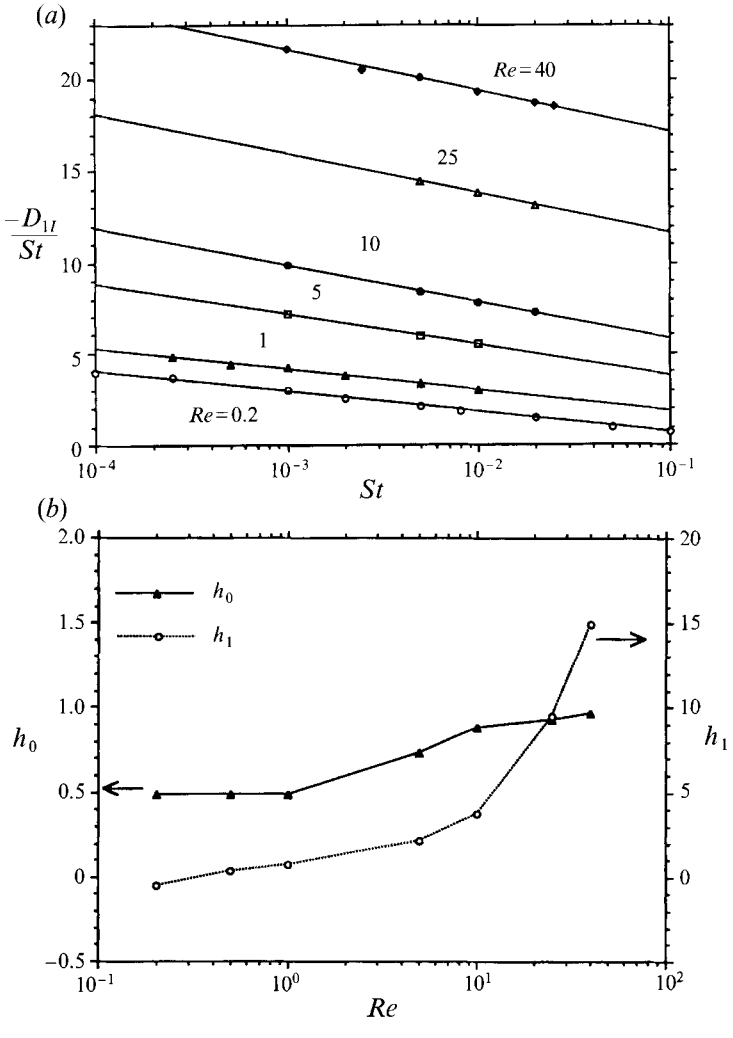

FIGURE 12. (*a*) Dependence of $-D_{1I}/St$ on $\log St$ at small St for $0.2 \leqslant Re \leqslant 40$. For small St, D_{1I}/St can be represented as $h_0 \log St - h_1$. (*b*) Dependence of h_0 and h_1 on Re in the purely oscillating flow.

the importance of the flow reversal on D_{1I}. For $\alpha_1 > \frac{2}{3}$, h_0 seems to level off which means that the oscillating component now dominates and the small mean component has little effect on h_0. In the SA case, $h_0 = 0$ and h_1 is linear in α_1 ($h_1/\alpha_1 \sim 0.804$ at $Re = 0.2$); thus the quantity h_1/α_1 is shown in figure 13(*b*). It is seen that h_1/α_1 is roughly a constant up to $\alpha_1 \sim 0.4$. For $0.8 < \alpha_1 < 1$, h_0 is roughly the same but h_1 decreases with decreasing α_1. Near $\alpha_1 = 0.5$, the numerical inaccuracy of h_1 may be the worst as h_1 changes sign quickly. Combining the behaviour of h_0 and h_1/α_1, it may be deduced that: (i) the logarithmic dependence of D_{1I} on St is a rule rather than an exception for an oscillating flow and the linear dependence of D_{1I} on St demonstrated in the SA case is actually an exception. (ii) For a fixed small but finite St, the theory developed for the SA case seems to describe, practically, the oscillating flow behaviour for α_1 up to 0.4 because h_0 is very small for small α_1.

Temkin & Kim (1980) argued that the changing wake structure significantly affects the unsteady drag. In the foregoing discussion for the low-frequency drag, it is seen

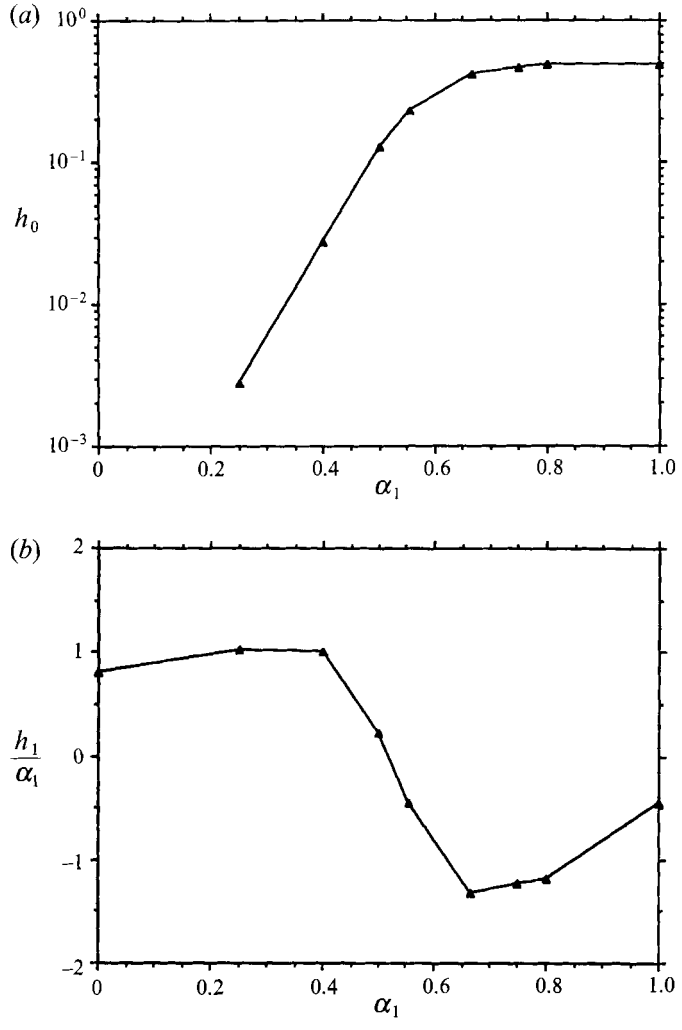

FIGURE 13. Dependence of h_0 and h_1 on the oscillating amplitude α_1 at $Re = 0.2$. The free-stream velocity is $U_\infty = U_0[1-\alpha_1+\alpha_1\cos t]$. Reynolds number is defined as $Re = U_0 2a/\nu$. The SA case (MLA 1991) is for $\alpha_1 \leqslant 1$ with $h_1 = 0$. (*a*) h_0; (*b*) h_1.

that the periodical flow reversal has no effect on the real components D_R but it does have some subtle effect on the imaginary component D_I. However, since D_I is very small for small St, it is not possible to measure any significant effect of the changing wake structure on the unsteady drag using an indirect measurement based on particle trajectories. At moderate and high values of ϵ, D_{1R} and D_{1I} behave the same as in the SA case, which suggests no effect on the drag caused by the changing wake structure due to flow reversal.

For a particle in a turbulent environment, it is difficult to determine α_1 especially if the flow is spatially inhomogeneous. Thus, it is impractical to devise an expression for the history force at finite Re that depends on α_1 explicitly. There are three possibilities to approximate the history force without involving α_1: (i) Basset's (1888) expression; (ii) the approximate expression derived by Mei & Adrian (1992) based on the SA case; (iii) an expression that is based on the current results of the PO case. From the Basset expression, $D_{1IH} \sim (\frac{1}{4}Re\,St)^{\frac{1}{2}}$. As $St \to 0$, $D_{1IH} \propto St$ for the SA case and

$D_{1IH} \sim h_0 St \log St - (h_1 - \frac{1}{6}Re)\, St$ for the PO case. As $St \to \infty$, all three give the same asymptotic value: $D_{1IH} \sim (\frac{1}{4}Re\, St)^{\frac{1}{2}}$. Although D_{1IH} of the PO case has a logarithmic dependence on St at small St, it is seen from figure 10(*b*) that D_{1IH} of the PO case is closer to that of the SA case than to the Stokes solution in the small St limit. Since it is difficult to develop an expression for $F'_H(t')$ at finite Re while the expression given by equations (6)–(8) has been tested for an impulsively started flow (Mei 1993 and LM), $F'_H(t')$ given by (6)–(8) is preferred. The error in predicting $F'_H(t')$ in the time domain for the PO case using (6)–(8) will be examined next in §4.4.

It is also interesting that the size of the computational domain r_E has such an important effect on the low-frequency drag. This suggests the following complicated long-time behaviour of the history force. In a dilute suspension, the particle mean-free path, λ, is not infinite. A 0.1 % concentration results in $\lambda/a \sim 10$. In a pipe flow, the ratio of the pipe diameter to particle size is not infinite either. These interactions may significantly reduce the long-time history force.

For the PO case one can also infer from $h_0(Re)$ and $h_1(Re)$ the limiting value of St below which the quasi-steady drag (2) is a good approximation for the unsteady drag owing to a purely oscillating flow around a sphere. For a given Re, one may neglect the history force and added-mass force when $|h_0 St \log St - h_1 St|/\phi < 0.01$. For $Re = 0.2$ and 40, the limiting values of St are 0.00484 and 0.0014, respectively.

4.4. *Assessment of the proposed particle dynamic equation at finite Re*

Even if one assumes that the approximation given by (6)–(8) can be used to represent $F'_H(t')$, the following questions arise immediately when u'_1 or v' is comparable to U': at which instant should u' and v' be used in (7) and which velocity should Re in (8) be based on? There are two relevant instants, t' and τ', in the integrand for the history force. Since the relative acceleration is evaluated at τ', we hypothesize that the velocities $u'(\tau')$ and $v'(\tau')$ be used in (7) and $Re(\tau')$ based on $|u'(\tau') - v'(\tau')|$ be used in (8). Combining the added-mass force derived by Auton *et al.* (1988) and Rivero *et al.* (1991), the modified history force, the quasi-steady force, and the body force, equation (9) is generalized to represent the total unsteady drag on a moving spherical particle,

$$F'(t) = \tfrac{4}{3}\pi a^3(\rho_p - \rho_f)\, g + 6\pi\rho_f \nu a(u' - v')\, \phi(t') + 6\pi\rho_f \nu a \int_{-\infty}^{t'} K(t' - \tau') \frac{\mathrm{d}(u' - v')}{\mathrm{d}\tau'} \mathrm{d}\tau' - \tfrac{2}{3}\rho_f \pi a^3 \frac{\mathrm{d}v'}{\mathrm{d}t'} + 2\rho_f \pi a^3 \frac{\mathrm{D}u'}{\mathrm{D}t'}, \quad (54)$$

with $\phi(t')$ given by (2*c*) or (2*e*–*i*) and $K(t' - \tau)$ given by

$$K(t' - \tau') \approx \left\{ \left[\frac{\pi(t' - \tau')\, \nu}{a^2} \right]^{\frac{1}{4}} + \left[\tfrac{1}{2}\pi \frac{|u'(\tau') - v'(\tau')|^3}{a\nu f_H^3(Re)} (t' - \tau')^2 \right]^{\frac{1}{2}} \right\}^{-2}, \quad (55)$$

where $$f_H(Re) = 0.75 + 0.105 Re(\tau'); \quad Re = |u'(\tau) - v'(\tau')| 2a/\nu. \quad (56)$$

In equation (54), u' and v' are the instantaneous velocities with no restrictions on the relative magnitude of the unsteady component compared to the steady or mean component. For two- or three-dimensional flows, generalization of (54) to a vector form may be possible but much remains to be investigated. For uniform flows, $\mathrm{D}u'/\mathrm{D}t' = \mathrm{d}u'/\mathrm{d}t'$ because the spatial derivatives vanish.

To assess the accuracy of equation (54), the following tests are conducted against numerical and experimental results for: (i) the PO case computed presently; (ii) the SA case; (iii) a sphere that possesses a large terminal velocity settling in a stagnant viscous

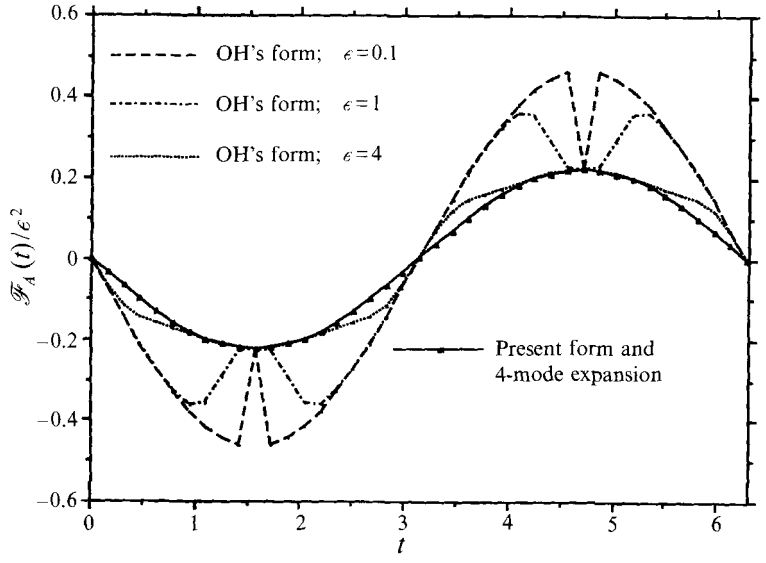

FIGURE 14. Comparison of the added-mass force between the present form and OH's form at $Re = 20$, $\epsilon = 0.1$, 1 and 4 for the PO case.

liquid with initially zero velocity. Comparisons are made for each component in addition to the total drag. Performance of the Basset's (1888) and OH's expressions for the history force and the added-mass force is also assessed.

In the PO and SA cases, the drag components are first normalized by $6\pi\rho_f \nu U_0 a$, where U_0 is the mean free-stream velocity in the SA case and the amplitude of the oscillating velocity in the PO case, respectively. Time is made dimensionless by the frequency of the oscillation ω. This results in the following,

$$\mathscr{F}_{QS}(t) = \phi(t)\, V(t), \tag{57}$$

$$\mathscr{F}_H(t) = \epsilon \int_{-\infty}^{t} K(t-\tau)\frac{\mathrm{d}V}{\mathrm{d}\tau}\mathrm{d}\tau, \tag{58}$$

$$\mathscr{F}_{AM}(t) = \tfrac{2}{9}\epsilon^2 \frac{\mathrm{d}V}{\mathrm{d}\tau}, \tag{59}$$

with

$$K(t-\tau) \approx (t-\tau)^{-\frac{1}{2}}\left\{(\tfrac{1}{2}\pi)^{\frac{1}{4}} + \left[\frac{\pi}{64}\left(\frac{Re(\tau)(t-\tau)^{\frac{1}{2}}}{\epsilon f_H(\tau)}\right)^3\right]^{\frac{1}{2}}\right\}^{-2}, \tag{60a}$$

$$Re(\tau) = U_0\, V(\tau)\, 2a/\nu, \quad f_H(\tau) = 0.75 + 0.105 Re(\tau), \tag{60b, c}$$

where $V(t) = \cos(t)$ for the PO case and $V(t) = 1+\beta\cos(t)$ for the SA case. The amplitude $\beta = 0.1$ is chosen in the SA case. Using Basset's (1888) expression, $\mathscr{F}_H(t) = \epsilon(\cos(t) - \sin(t))$ and $\mathscr{F}_H(t) = \beta\epsilon(\cos(t) - \sin(t))$ are obtained for the PO and SA cases, respectively. The added-mass force in Basset's solution and the presently proposed form is $\mathscr{F}_{AM}(t) = -\frac{2}{9}\epsilon^2 \sin(t)$ for the PO case.

4.4.1. *The PO case*

Figure 14 compares the added-mass force, scaled by ϵ^2, of the present form, (59), with that of OH, (48), for the PO case at $Re = 20$ and $\epsilon = 0.1$, 1 and 4. The added-mass force based on OH's form exhibits a peculiar behaviour near the point of maximum

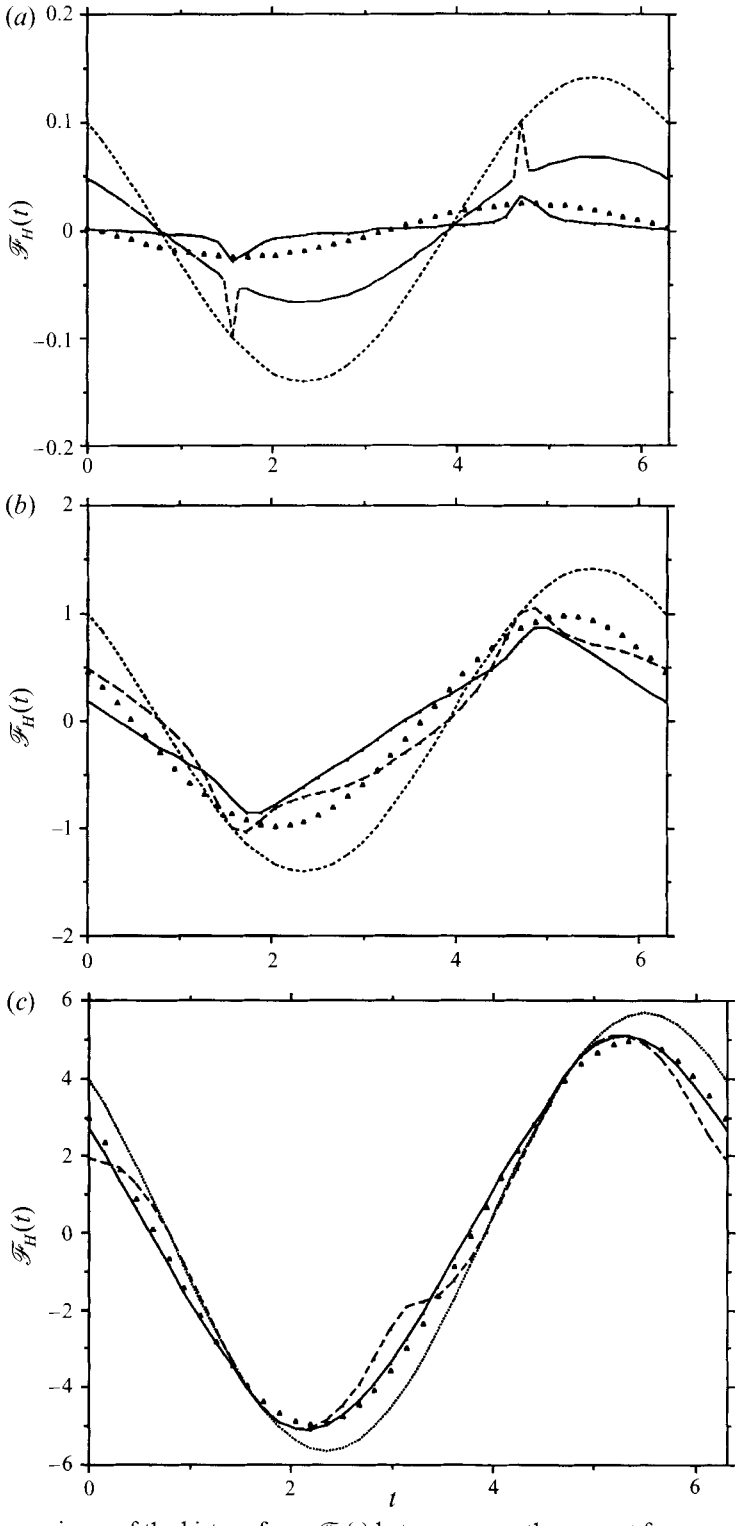

FIGURE 15. Comparisons of the history force $\mathscr{F}_H(t)$ between ——, the present form; – – –, OH's form, and the numerical results for the PO case. ...., Basset (1888); ▲, 4-mode expansion. (*a*) $(Re, \epsilon) = (20, 0.1)$; (*b*) $(Re, \epsilon) = (20, 1)$; (*c*) $(Re, \epsilon) = (20, 4)$.

acceleration or zero velocity. The added-mass force drops rapidly when $V(t) = 0$ for small ϵ. This type of peculiarity has no known physical basis. It exists because the correction coefficient C_A was not determined on physical grounds. At $\epsilon = 4$, that corresponds to the high-frequency limit, this peculiar behaviour almost disappears because the unsteady flow approaches the Stokes flow limit and little correction needs to be applied to the history force and the added-mass force. Although equations (3)–(5) and (47) were based on the experimental results of the PO case, the performance is not satisfactory. On the other hand, the present form for the added-mass is well behaved.

The history force $\mathscr{F}_H(t)$ is the most difficult component to represent accurately. Figure 15 compares three forms of the history force at $Re = 20$, $\epsilon = 0.1$, 1 and 4: OH's form (47), the present form (58) and (60), and the present numerical result based on the first mode, D_{1RH} and D_{1IH}. The Stokes number ϵ is chosen to cover small, intermediate and 'high' frequencies. For $\epsilon \ll 1$, the third mode, mainly the imaginary component D_{3IH}, is not entirely negligible in comparison with D_{1IH}. Thus the numerical result for $\mathscr{F}_H(t)$ based on D_{1RH} and D_{1IH} for $\epsilon = 0.1$ suffers slight inaccuracy. For $\epsilon = 1$ and 4, D_{1RH} and D_{1IH} are the dominant part of the history force because the higher modes are small. It is seen that OH's form over-predicts $\mathscr{F}_H(t)$ at low frequency, $\epsilon = 0.1$, while the present form slightly under-predicts $\mathscr{F}_H(t)$ since it is known to give a lower value. Also shown in figure 15(*a*) is the prediction using the classical Basset force expression (Basset 1888). The classical form grossly over-predicts $\mathscr{F}_H(t)$ at finite Re. Similar to the added-mass force of the OH's form, a large spike appears in $\mathscr{F}_H^{OH}(t)$ at $t = \frac{1}{2}\pi$ when $V(t) = 0$. At $\epsilon = 4$, the present form agrees well with the numerical result while OH's form still exhibits some peculiarity near $t = \pi$ when the acceleration is zero. At $\epsilon = 1$, both forms have similar inaccuracy compared with the numerical results. This persists at higher Re. The comparison for total drag between the prediction based on (54) and the numerical solution at $(Re, \epsilon) = (40, 1)$ and $(40, 4)$ has been shown in figure 8; and the error in the total drag at $\epsilon = 1$ using (54) is due to the inaccuracy of $\mathscr{F}_H(t)$. Figure 8(*a*) actually shows the worst case since this error vanishes when ϵ is small because $\mathscr{F}_H(t) \propto \epsilon^2$ as ϵ approaches zero. The error also vanishes for large ϵ, as shown in figure 8(*b*), because the present form approaches the high-frequency limit correctly. The seemingly good agreement at $\epsilon = 1$ between the experimental results and the prediction using OH's form stems from the fact that OH's form has errors in both expressions for the added-mass force and the history force. These errors happen to cancel each other in the PO case. It is noted that the expression give by (60) is based on $f_H(Re)$ derived from the SA case assuming a constant Re. The comparisons shown in figure 15 are rather encouraging since $\mathscr{F}_H(t)$ given by (6)–(8) appears robust in its application to the PO case.

4.4.2. *The SA case*

Figure 16 compares $\mathscr{F}_H(t)$ at $Re = 40$ and $\epsilon = 1.0$ for the SA case with $\beta = 0.1$. Here, Re is based on the mean free-stream velocity. Clearly, both OH's and Basset's forms over-predict $\mathscr{F}_H(t)$ and both have large phase errors indicated by the locations of the maximum in $\mathscr{F}_H(t)$. The present form agrees very well with the numerical results because $\mathscr{F}_H(t)$ is constructed from the results of the SA case.

4.4.3. *A sphere settling in a stagnant viscous fluid*

Moorman (1955) conducted a series of careful experiments for a sphere settling in a quiescent fluid. The Reynolds number Re_T (based on the diameter and the actual terminal velocity V_T) spans a large range. The density ratio $\rho = \rho_p/\rho_f$ of the particle to fluid ranges from 1.17 to 9.15. To predict the velocity history of the settling sphere, time

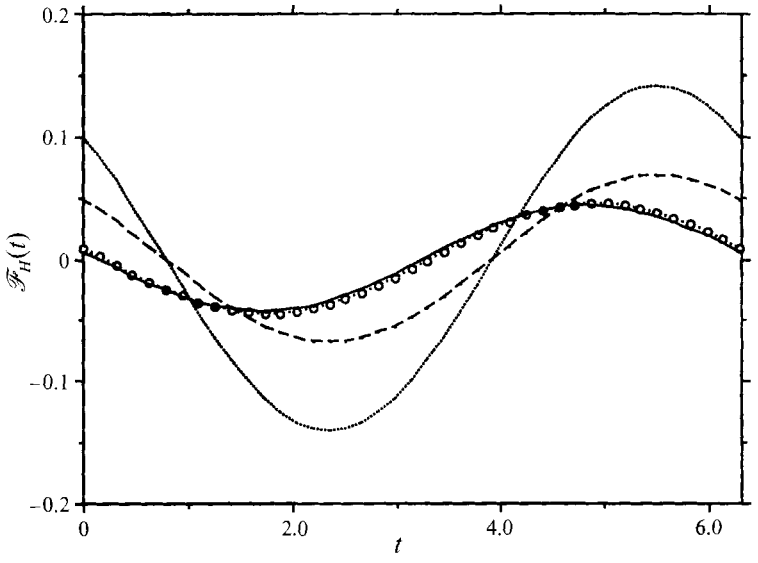

FIGURE 16. Comparisons of the history force $\mathscr{F}_H(t)$ between ——, the present form, – – –, OH's form, and the computed results for the SA case at $(Re, \epsilon) = (40, 1)$, amplitude = 0.1...., Basset (1888); ○, MLA (1991).

and velocity are made dimensionless by the diffusional timescale a^2/ν and the nominal terminal velocity $V_{TS} = 2(\rho-1)a^2g/9\nu$ obtained by balancing the body force and Stokes drag. This results in:

$$\frac{2(\rho+0.5)}{9}\frac{\mathrm{d}V}{\mathrm{d}t} = 1-\phi V(t)-\int_0^t K(t-\tau)\frac{\mathrm{d}V}{\mathrm{d}\tau}\mathrm{d}\tau, \tag{61}$$

where the body force and the quasi-steady force are $\mathscr{F}_{G-B} = 1$ and $\mathscr{F}_{QS}(t) = -\phi V(t)$ after they are normalized by $6\pi\rho_f \nu V_{TS} a$. The last term is the history force whose kernel is

$$K(t-\tau) = (\pi(t-\tau))^{-\frac{1}{2}}\{1+[\tfrac{1}{256}\pi(Re(\tau)(t-\tau)^{\frac{1}{2}}/f_H(\tau))^6]^{\frac{1}{6}}\}^{-2}. \tag{62}$$

The added-mass force, normalized by $6\pi\rho_f \nu V_{TS} a$, is

$$\mathscr{F}_{AM}(t) = -\frac{1}{9}\frac{\mathrm{d}V}{\mathrm{d}t}, \tag{63}$$

that has been incorporated on the left-hand side of (61). It is noted that Re and f_H are evaluated at τ in (62). The following data in Moorman (1955) are selected: $(Re_T, \rho) = (28.57, 2.467)$, $(48.787, 1.267)$, and $(331.45, 2.573)$ (they correspond to Run 27, Run 36, and Run 33, respectively) because these cases have enough data points to reach $V/V_T \sim 1$ and the Reynolds numbers are representative of moderate and high values.

Figure 17 compares the settling velocity history $v(t)/V_T$ computed using OH's form, the classical representations for the Basset history force and added-mass force (Basset 1888), and the present particle dynamic equation with experimental result (Moorman 1955) for $Re_T = 28.57$, 48.78 and 331.45. Close agreement between the measured and the predicted values (based on equation (54)) is observed for all three cases, especially at the later stage when v approaches V_T and the unsteady forces are supposed to be small. OH's form gives a smaller velocity than the measurement for $t \sim 1$. Noting that

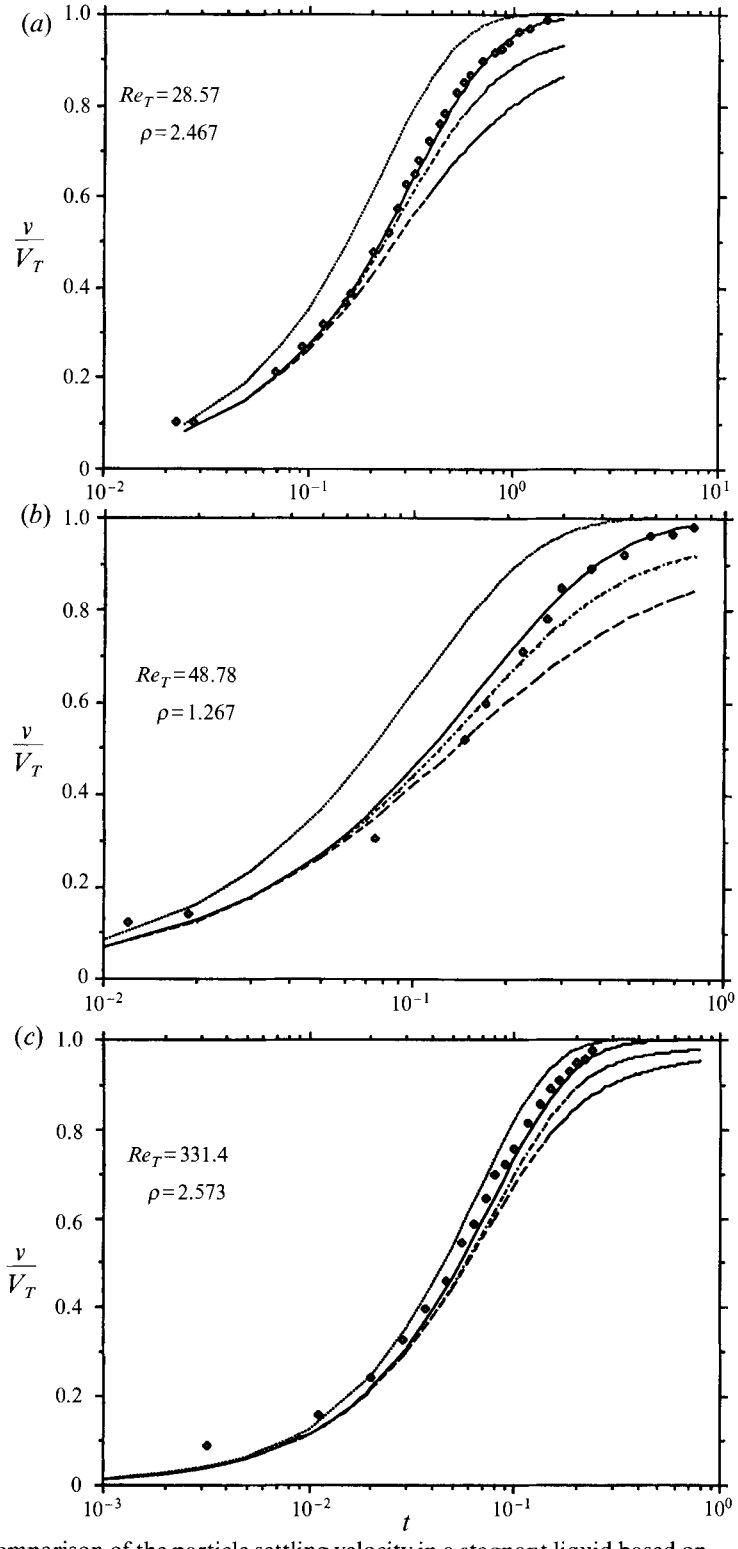

FIGURE 17. Comparison of the particle settling velocity in a stagnant liquid based on ——, the present form, – – –, the Basset (1888) solution and —·—·—, OH's form. (*a*) $(Re_T, \rho) = (28.57, 2.467)$; (*b*) $(Re_T, \rho) = (48.78, 1.267)$; (*c*) $(Re_T, \rho) = (331.45, 2.573)$. ◇, Moorman (1955); ...., no history force.

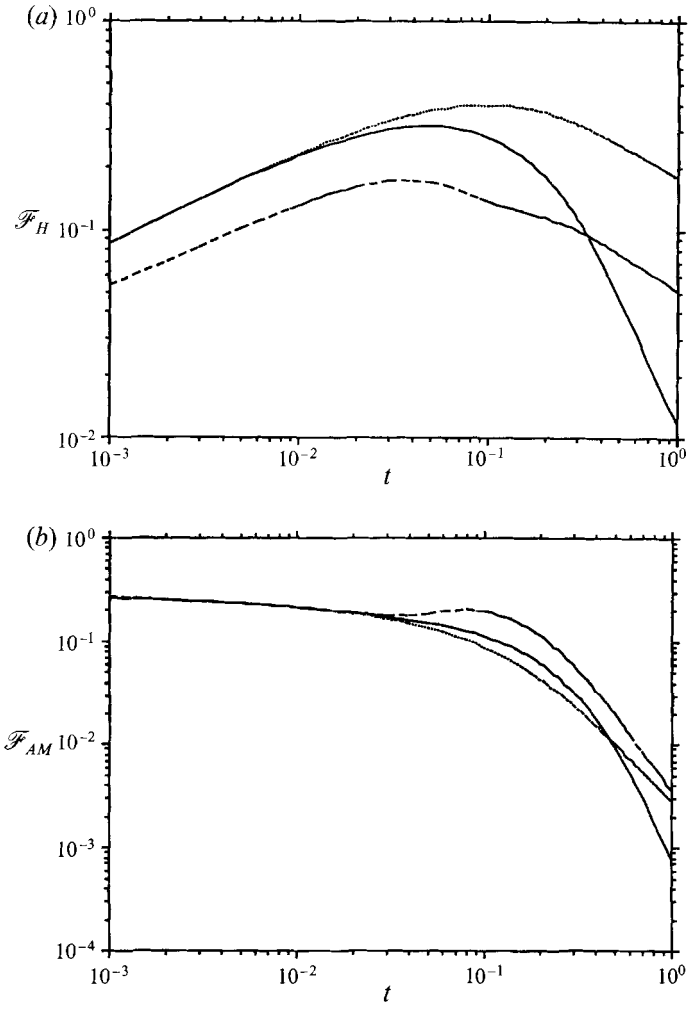

FIGURE 18. History force and added-mass force on the settling sphere for $(Re_T, \rho) = (48.78, 1.267)$. (*a*) History force; (*b*) added-mass force. ...., Basset (1888); – –, OH (1964); ——, present prediction.

the acceleration parameter defined in (5) ranges from zero to infinity and $Re(t)$ ranges from 0 to Re_T as high as 331.45, which is beyond the range investigated in this study and in Mei & Adrian (1992) for the SA case, the present particle dynamics equation does capture the transient variation of the particle velocity quite well.

It is instructive to examine the behaviour of $\mathscr{F}_{AM}(t)$ and $\mathscr{F}_H(t)$ during the transient passage. Figure 18 compares $\mathscr{F}_{AM}(t)$ and $\mathscr{F}_H(t)$ for $0 < t < 1$ based on OH's form, the present form and the classical form of Basset (1888) for $Re_T = 48.78$. The comparisons are shown only for this period of time because the experimental data for v/V_T exist only for $t < 0.8$ for this case. Furthermore, $\mathscr{F}_H(t)$ given by (6)–(8) is only a rough approximation and should not be viewed as exact. It is seen that the added-mass force $\mathscr{F}_{AM}(t)$ of OH's form decreases first and then peaks at some later time, which again has no known physical basis. The present form predicts monotonically decreasing $\mathscr{F}_{AM}(t)$ that is close to the prediction based on Basset's representations for $\mathscr{F}_H(t)$ and $\mathscr{F}_{AM}(t)$. For $\mathscr{F}_H(t)$, the classical form and OH's form predict a $t^{-\frac{1}{2}}$-decay for $\mathscr{F}_H(t)$ for $t \sim O(1)$. It is seen that the presently predicted $\mathscr{F}_H(t)$ decays much faster than the other two

forms at $t \sim 1$. By linearizing equation (61) near $v = V_T$, it can be shown that $1 - v(t)/V_T$ is proportional to $\mathscr{F}_H(t)$. Thus the settling velocity $v(t)$ given by the present particle dynamic equation should approach V_T faster than the other two. This is consistent with what is shown in figure 17.

Finally, it must be emphasized that the proposed particle dynamic equation is only, strictly speaking, applicable to spatially uniform unsteady flows. For non-uniform viscous flows, uncertainty remains on how best to represent the contribution to the drag owing to the spatial acceleration. More discussions can be found, for example, in the work of Auton *et al.* (1988) for particle motion in inviscid flows.

5. Conclusions

(i) Numerical solution, together with a high-frequency asymptotic solution, of the unsteady Navier–Stokes equation has been obtained for flow over a stationary sphere at finite Reynolds number with oscillating free-stream velocity. The total unsteady drag computed compares well with Odar & Hamilton's (1964) experimental results at finite Re. Various unsteady drag components are examined.

(ii) The flow field at $St \ll Re \ll 1$ exhibits a triple-region structure: an inner Stokes region $r \sim O(1)$, an intermediate Oseen region $r \sim O(Re^{-1})$, and an outer region $x \sim O(St^{-1}), y \sim O(\epsilon^{-1})$. In the inner region, the flow is governed by the quasi-steady Stokes equation. In the Oseen region, the flow is governed, to the leading order, by the quasi-steady Oseen equation. In the outer region, the flow is governed by an unsteady convection–diffusion process.

(iii) The history force at finite Re is linearly proportional to $\omega^{\frac{1}{2}}$ only at high frequency. For $St \ll Re$ or $St \ll 1$, the imaginary component of the drag has a logarithmic dependence on St, $D_{1I} \sim (h_0\, St \log St - h_1\, St)$. This is confirmed also by the analytical results of Lovalenti & Brady (1993*a*). As Re increases, h_1 increases nearly linearly while h_0 seems to level off. Thus the logarithmic dependence of the drag on St is relatively weaker at higher Re than at small Re. For a mean flow imposed with a fluctuation, $U_0(1-\alpha_1+\alpha_1\cos\omega t')$, h_0 decreases rapidly to zero as $\alpha_1 \to 0$ and the SA case investigated by MLA (1991) is recovered.

(iv) A general particle dynamic equation including the quasi-steady drag, history force and added-mass force in the time domain is proposed for particle motions at finite Reynolds number. The present form for the history force performs consistently better than that of Odar & Hamilton (1964) at finite Re when tested against the numerical results of the SA case and the PO case. The predicted velocity of a settling sphere with large terminal velocity in a quiescent fluid is in close agreement with the experimentally measured values (Moorman 1955).

The author is grateful to reviewers for their many useful criticisms and comments that led to the improvement of the paper.

Appendix. Asymptotic solution for the oscillating flow at finite Reynolds number and high frequency

The governing equation for the stream function ψ given by (10) can be rewritten, for convenience, as,

$$\frac{\partial}{\partial t}(\mathrm{D}^2\psi) + \frac{1}{St}\left[\frac{1}{r^2}\frac{\partial(\psi, \mathrm{D}^2\psi)}{\partial(r,\mu)} + \frac{2}{r^2}\mathrm{D}^2\psi L_r\psi\right] = \frac{1}{St\,Re}\mathrm{D}^4\psi, \tag{A 1}$$

where $Re' = \frac{1}{2}Re$, $\mu = \cos\theta$, $\mathrm{D}^2 = \dfrac{\partial^2}{\partial r^2} + \dfrac{1-\mu^2}{r^2}\dfrac{\partial^2}{\partial \mu^2}$, $L_r = \dfrac{\mu}{1-\mu^2}\dfrac{\partial}{\partial r} + \dfrac{1}{r}\dfrac{\partial}{\partial \mu}$. (A 2)

The no-slip condition on the wall is specified and the boundary condition at infinity for the oscillating flow is,

$$\psi \to \tfrac{1}{2}r^2(1-\mu^2)\,\mathrm{e}^{-\mathrm{i}t} \quad \text{as } r \to \infty. \tag{A 3}$$

Only real values are physically significant.

Wang (1968) has shown that the stream function ψ for a high-frequency flow over a cylinder can be represented as

$$\psi = \tilde{\psi} + St^{-1}\bar{\psi} \tag{A 4}$$

where $\tilde{\psi}$ and $\bar{\psi}$ are the unsteady and steady components of the stream function, respectively, and they are both order one quantities. The steady component is a consequence of the purely oscillating flow setting up a steady streaming motion resulting from the nonlinearity of the governing equation. The important feature of (A 3) is that the steady component is scaled as St^{-1}. An examination of (A 1) shows that (A 4) is also valid for a high-frequency oscillating flow over a sphere. Defining

$$\delta = St^{-\frac{1}{2}} \ll 1, \quad \alpha = Re'^{-1}, \tag{A 5}$$

where α is a constant of order unity, and recalling that $g = \mathrm{D}^2\psi$, (A 1) becomes

$$\frac{\partial \tilde{g}}{\partial t} - \alpha\delta^2\mathrm{D}^2\tilde{g} = -\delta^4\left[\frac{1}{r^2}\frac{\partial(\bar{\psi},\tilde{g})}{\partial(r,\mu)} + \frac{2}{r^2}\tilde{g}L_r\bar{\psi} + \frac{1}{r^2}\frac{\partial(\tilde{\psi},\bar{g})}{\partial(r,\mu)} + \frac{2}{r^2}\bar{g}L_r\tilde{\psi}\right] - \delta^2\left[\frac{1}{r^2}\frac{\partial(\tilde{\psi},\tilde{g})}{\partial(r,\mu)} + \frac{2}{r^2}\tilde{g}L_r\tilde{\psi}\right]_u, \tag{A 6}$$

$$\alpha\delta^2\mathrm{D}^2\bar{g} = \delta^4\left[\frac{1}{r^2}\frac{\partial(\bar{\psi},\bar{g})}{\partial(r,\mu)} + \frac{2}{r^2}\bar{g}L_r\bar{\psi}\right] + \delta^2\left[\frac{1}{r^2}\frac{\partial(\tilde{\psi},\tilde{g})}{\partial(r,\mu)} + \frac{2}{r^2}\tilde{g}L_r\tilde{\psi}\right]_s, \tag{A 7}$$

where the subscripts u and s denote the unsteady and steady parts of the nonlinear term. Equations (A 6)–(A 7) constitute the basis for an asymptotic expansion.

Starting from the outer region of $r-1 \sim O(1)$, the outer solutions for g and ψ can be expressed as

$$G = G_0 + \delta G_1 + \delta^2 G_2 + \delta^3 G_3 + \delta^4 G_4 + \ldots, \tag{A 8}$$

$$\Psi = \Psi_0 + \delta\Psi_1 + \delta^2\Psi_2 + \ldots, \tag{A 9}$$

(A 6) and (A 8)–(A 9) give,

$$\tilde{G}_0 = \tilde{G}_1 = \tilde{G}_2 = \tilde{G}_3 = 0, \tag{A 10}$$

$$\frac{\partial \tilde{g}_4}{\partial t} = -\left[\frac{1}{r^2}\frac{\partial(\tilde{\psi}_0,\bar{G}_0)}{\partial(r,\mu)} + \frac{2}{r^2}\bar{G}_0L_r\tilde{\psi}_0\right]. \tag{A 11}$$

The steady component of g is governed by

$$\mathrm{D}^2\bar{G}_0 = \mathrm{D}^2\bar{G}_1 = 0, \tag{A 12}$$

$$\alpha\mathrm{D}^2\bar{G}_2 = \left[\frac{1}{r^2}\frac{\partial(\bar{\Psi}_0,\bar{G}_0)}{\partial(r,\mu)} + \frac{2}{r^2}\bar{G}_0L_r\bar{\Psi}_0\right] + \left[\frac{1}{r^2}\frac{\partial(\tilde{\Psi},\bar{G}_4)}{\partial(r,\mu)} + \frac{2}{r^2}\bar{G}_4L_r\tilde{\Psi}_0\right]_s, \tag{A 13}$$

which implies that the equations governing $\bar{\Psi}_m$ and $\tilde{\Psi}_m$ are $\mathrm{D}_r^2\bar{\Psi}_m = 0$ for $m = 0$ and 1, and $\mathrm{D}^2\tilde{\Psi}_m = 0$ for $m = 0$, 1, 2 and 3. Stretching the coordinate near the wall,

$$\eta = (r-1)/\delta\alpha^{\frac{1}{2}}, \tag{A 14}$$

and expressing the inner solution in the form of

$$\psi = \delta\psi_0 + \delta^2\psi_1 + \delta^3\psi_2 + \ldots, \tag{A 15}$$

the following equations are obtained,

$$\left(\frac{\partial}{\partial t} - \frac{\partial^2}{\partial \eta^2}\right)\frac{\partial^2}{\partial \eta^2}\tilde{\psi}_0 = 0, \tag{A 16}$$

$$\left(\frac{\partial}{\partial t} - \frac{\partial^2}{\partial \eta^2}\right)\frac{\partial^2}{\partial \eta^2}\tilde{\psi}_1 = 0, \tag{A 17}$$

$$\left(\frac{\partial}{\partial t} - \frac{\partial^2}{\partial \eta^2}\right)\frac{\partial^2}{\partial \eta^2}\tilde{\psi}_2 = \alpha(1-\mu^2)\left(2\frac{\partial^4 \tilde{\Psi}_0}{\partial \eta^2 \partial \mu^2} - \frac{\partial^3 \tilde{\psi}_0}{\partial t \partial \mu^2}\right) - \alpha^{-\frac{1}{2}}\left[\frac{\partial \tilde{\psi}_0}{\partial \eta}\frac{\partial^3 \tilde{\psi}_0}{\partial \mu \partial \eta^2} - \frac{\partial \tilde{\psi}_0}{\partial \mu}\frac{\partial^3 \tilde{\psi}_0}{\partial \eta^3} + \frac{2\mu}{1-\mu^2}\frac{\partial \tilde{\psi}_0}{\partial \eta}\frac{\partial^2 \tilde{\psi}_0}{\partial^2 \eta}\right]_u, \tag{A 18}$$

$$\frac{\partial^4}{\partial \eta^4}\bar{\psi}_0 = \alpha^{-\frac{1}{2}}\left[\frac{\partial \tilde{\psi}_0}{\partial \eta}\frac{\partial^3 \tilde{\psi}_0}{\partial \mu \partial \eta^2} - \frac{\partial \tilde{\psi}_0}{\partial \mu}\frac{\partial^3 \tilde{\psi}_0}{\partial \eta^3} + \frac{2\mu}{1-\mu^2}\frac{\partial \tilde{\psi}_0}{\partial \eta}\frac{\partial^2 \tilde{\psi}_0}{\partial^2 \eta}\right]_s. \tag{A 19}$$

Solving and matching the solutions in the following order,

$$\Psi_0 \to \tilde{\psi}_0 \to \tilde{\Psi}_1 \to \tilde{\psi}_1 \to \tilde{\Psi}_2 \to \tilde{\psi}_{21}, \quad \tilde{\psi}_0 \to (\bar{\psi}_0 \text{ and } \tilde{\psi}_{22}) \to (\bar{\Psi}_0 \text{ and } \tilde{\Psi}_3),$$

where $\tilde{\psi}_{21}$ and $\tilde{\psi}_{22}$ are the $O(\delta^3)$ term in (A 15) and are associated with the single and double harmonics e^{-it} and e^{-i2t}, respectively, the solutions to various orders in inner and outer regions are readily obtained

$$\tilde{\Psi}_0 = \tfrac{1}{2}(r^2 - r^{-1})(1-\mu^2)\,e^{-it}, \tag{A 20}$$

$$\tilde{\psi}_0 = \tfrac{3}{2}\alpha^{\frac{1}{2}}(1-\mu^2)\,e^{-it}[\eta + [(1+i)/\sqrt{2}](E-1)], \tag{A 21}$$

$$\tilde{\Psi}_1 = -\tfrac{3}{4}(2\alpha)^{\frac{1}{2}}(1+i)[(1-\mu^2)/r]\,e^{-it}, \tag{A 22}$$

$$\tilde{\psi}_1 = \tfrac{3}{4}2^{\frac{1}{2}}\alpha(1+i)(1-\mu^2)\,e^{-it}[\eta + [(1+i)/\sqrt{2}](E-1)], \tag{A 23}$$

$$\tilde{\Psi}_2 = i\tfrac{3}{2}\alpha[(1-\mu^2)/r]\,e^{-it}, \tag{A 24}$$

$$\tilde{\psi}_{21} = 3\alpha^{\frac{3}{2}}(1-\mu^2)\,e^{-it}[-\tfrac{1}{2}i\eta E + \tfrac{1}{6}\eta^3 - \tfrac{1}{4}\sqrt{2}(1+i)\mu^2 + \tfrac{1}{2}i\eta), \tag{A 25}$$

$$\tilde{\psi}_{22} = \tfrac{9}{8}\alpha^{\frac{1}{2}}\mu(1-\mu^2)\,e^{-i2t}\left[\frac{1-i}{\sqrt{2}}E + \frac{1-i}{8\sqrt{2}}E^2 + i\eta E + \tfrac{9}{8}\left(1-\frac{1}{\sqrt{2}}\right)(1-i)(1-E^{\sqrt{2}})\right], \tag{A 26}$$

$$\bar{\psi}_0 = \tfrac{9}{8}\alpha^{\frac{1}{2}}\mu(1-\mu^2)[2\eta\exp(-\eta/\sqrt{2})\sin(\eta/\sqrt{2}) + \tfrac{1}{4}\sqrt{2}\exp(-\sqrt{2}\eta] + 5\sqrt{2}\exp\left(-\frac{\eta}{\sqrt{2}}\right)\cos\left(\frac{\eta}{\sqrt{2}}\right) + 3\sqrt{2}\exp\left(-\frac{\eta}{\sqrt{2}}\right)\sin\left(\frac{\eta}{\sqrt{2}}\right) + \tfrac{5}{2}\eta - \tfrac{21}{4}\sqrt{2}\Big], \tag{A 27}$$

$$\bar{\Psi}_0 = \tfrac{45}{32}\mu(1-\mu^2)(1-r^{-2}), \tag{A 28}$$

$$\tilde{\Psi}_3 = \frac{9}{64}\left(1-\frac{1}{\sqrt{2}}\right)(1-i)\,\alpha^{\frac{1}{2}}\frac{\mu(1-\mu^2)}{r^2}e^{-i2t}, \tag{A 29}$$

where

$$E = \exp(-[(1-i)/\sqrt{2}]\,\eta), \tag{A 30}$$

and $1-\mu^2 \equiv \sin^2\theta$. The solutions given by (A 20)–(A 29) have the following physical interpretation, that is not obvious from the unsteady Stokes solution. The outer solution $\tilde{\Psi}_0$ is a potential flow oscillating around the sphere driven by the free-stream condition and $\tilde{\psi}_0$ describes the boundary-layer flow driven by the outer potential flow

$\tilde{\Psi}_0$. The $O(1)$ term at large η in $\tilde{\psi}_0$ reflects the viscous displacement effect that results in $\tilde{\Psi}_1$ which is an oscillating doublet in the outer region. This doublet in turn induces a second-order boundary-layer flow, $\tilde{\psi}_1$, in the inner region. The $O(1)$ term in $\tilde{\psi}_1$ at large η again is the viscous displacement effect that induces a second-order doublet $\tilde{\psi}_2$. The solution $\tilde{\psi}_{21}$ accounts for the curvature effect, as indicated by the first term on the right-hand side of (A 18), on $O(\delta^3)$ level. The other $O(\delta^3)$ terms, $\tilde{\psi}_{22}$ and $\bar{\psi}_0$, are the consequences of the nonlinearity. Since $\tilde{\psi}_{21}$ has no $O(1)$ term at large η, there is no $\tilde{\Psi}_{31}$ term associated with the first harmonic in the outer region and $\tilde{\Psi}_3$, an oscillating quadruple, is caused by the viscous displacement effects in $\tilde{\psi}_{22}$. The steady outer solution $\bar{\Psi}_0$ does not decay at infinity and its presence can be easily visualized in the experiments investigating the steady streaming.

The function g_1 defined by (16*b*) can be evaluated from (A 21), (A 23), and (A 25) since g_1 is zero in the outer region. It is given by

$$e^{-it}g_1 = e^{-it}(1-\mu^2)\frac{1}{\delta\alpha^{\frac{1}{2}}}\frac{3}{2}\left(\frac{1-i}{\sqrt{2}}+\delta\alpha^{\frac{1}{2}}-\delta^2\alpha\eta\right)E, \tag{A 31}$$

which is $D^2\tilde{\psi}$ associated with the fundamental mode.

REFERENCES

ANDERSON, D. A., TENNEHILL, J. C. & FLETCHER, R. H. 1984 *Computational Fluid Mechanics and Heat Transfer*. McGraw-Hill.

AUTON, T. R., HUNT, J. C. R. & PRUD'HOMME, M. 1988 The force exerted on a body in inviscid unsteady non-uniform rotational flow. *J. Fluid Mech.* **197**, 241–257.

BASSET, A. B. 1888 *A Treatise On Hydrodynamics*, vol. 2. Dover.

BRILEY, M. R. 1971 A numerical study of laminar separation bubbles using the Navier–Stokes equations. *J. Fluid Mech.* **47**, 713–736.

CLIFT, R., GRACE, J. R. & WEBER, M. E. 1978 *Bubbles, Drops and Particles*. Academic.

DRUMMOND, K. C. & LYMAN, F. A. 1990 Mass transfer from a sphere in an oscillating flow with zero mean velocity. *Comput. Mech.* **6**, no. 4, 315–326.

KARANFILIAN, S. K. & KOTAS, T. J. 1978 Drag on a sphere in unsteady motion in a liquid at rest. *J. Fluid Mech.* **87**, 88–96.

KIM, I. & PEARLSTEIN, A. J. 1990 Stability of the flow past a sphere. *J. Fluid Mech.* **211**, 73–93.

LANDAU, L. E. & LIFSHITZ, E. M. 1959 *Fluid Mechanics*. Pergamon.

LAWRENCE, C. J. & MEI, R. 1994 Long-time behaviour of the drag on a body in impulsive motion. *J. Fluid Mech.* (in press).

LINTERIS, G. T., LIBBY, P. A. & WILLIAMS, F. A. 1991 Droplet dynamics in a non-uniform field. *Combust. Sci. Tech.* **80**, 319–335.

LOVALENTI, P. M. & BRADY, J. F. 1993*a* The hydrodynamic force on a rigid particle undergoing arbitrary time-dependent motion at small Reynolds number. *J. Fluid Mech.* **256**, 561–605.

LOVALENTI, P. M. & BRADY, J. F. 1993*b* The force on a sphere in a uniform flow with small-amplitude oscillations at finite Reynolds number. *J. Fluid Mech.* **256**, 607–614.

MAXEY, M. R. & RILEY, J. J. 1983 Equation of motion for a small rigid sphere in a nonuniform flow. *Phys. Fluids* **26** (4), 863–889.

MEI, R. 1990 Particle dispersion in isotropic turbulence and unsteady particle dynamics at finite Reynolds number. PhD thesis, University of Illinois at Urbana-Champaign, Urbana, IL.

MEI, R. 1993 History force on a sphere due to a step change in the free-stream velocity. *Intl J. Multiphase Flow* **19** (3), 509–525.

MEI, R. & ADRIAN, R. J. 1992 Flow past a sphere with an oscillation in the free-stream and unsteady drag at finite Reynolds number. *J. Fluid Mech.* **237**, 323–341.

MEI, R., LAWRENCE, C. J. & ADRIAN, R. J. 1991 Unsteady drag on a sphere at finite Reynolds number with small fluctuations in the free-stream velocity. *J. Fluid Mech.* **233**, 613–631.

MEI, R. & PLOTKIN, A. 1986*a* A finite difference scheme for the solution of the steady Navier–Stokes equation. *Comput. Fluids* **14**, 239–251.

MEI, R. & PLOTKIN, A. 1986*b* Navier–Stokes solution for some laminar incompressible flows with separation in forward facing step geometries. *AIAA J.* **24** (7), 1106–1111.

MOORMAN, R. W. 1955 Motion of a spherical particle in the accelerated portion of free fall. PhD thesis, University of Iowa, Iowa.

ODAR, F. 1966 Verification of the proposed equation for calculation of the forces on a sphere accelerating in a viscous fluid. *J. Fluid Mech.* **25**, 591–592.

ODAR, F. & HAMILTON, W. S. 1964 Forces on a sphere accelerating in a viscous fluid. *J. Fluid Mech.* **18**, 302–314.

PROUDMAN, I. & PEARSON, J. R. A. 1957 Expansions at small Reynolds numbers for the flow past a sphere and a circular cylinder. *J. Fluid Mech.* **2**, 237–262.

REEKS, M. W. & MCKEE, S. 1984 The dispersive effects of Basset history forces on particle motion in a turbulent flow. *Phys. Fluids* **27** (7), 1573–1582.

RILEY, N. 1966 On a sphere oscillating in a viscous fluid. *Q. J. Mech. Appl. Maths* **19**, 461–472.

RIVERO, M., MAGNAUDET, J. & FARBE, J. 1991 Quelques résultalts nouveaux concernant les forces exercées sur une inclusion sphérique par ecoulement accéléré (New results on the forces exerted on a spherical body by an accelerated flow). *C.R. Acad. Sci. Paris* **312**, Sér. II, 1499–1506.

SANO, T. 1981 Unsteady flow past a sphere at low Reynolds number. *J. Fluid Mech.* **112**, 433–441.

SCHÖNEBORN, P.-R. 1975 The interaction between a single particle and oscillating fluid. *Intl J. Multiphase Flow* **2**, 307–317.

STOKES, G. G. 1851 On the effect of internal friction of fluids on the motion of pendulum. *Trans. Camb. Phil. Soc.* **9**, 8. Reprinted in *Mathematics and Physics Papers III*, Cambridge University Press (1922).

TEMKIN, S. & KIM, S. S. 1980 Droplet motion induced by weak shock waves. *J. Fluid Mech.* **96**, 133–157.

TEMKIN, S. & MEHTA, H. K. 1982 Droplet drag in an accelerating and decelerating flow. *J. Fluid Mech.* **116**, 297–313.

TSUJI, Y., KATO, N. & TANAKA, T. 1991 Experiments on the unsteady drag and wake of a sphere at high Reynolds numbers. *Intl J. Multiphase Flow* **17** (3), 343–354.

WANG, C.-Y. 1968 On high-frequency oscillatory flows. *J. Fluid Mech.* **32**, 55–68.